

ENSO Modulation of the QBO: Results from MIROC Models with and without Nonorographic Gravity Wave Parameterization

YOSHIO KAWATANI,^a KEVIN HAMILTON,^{b,c} KAORU SATO,^d TIMOTHY J. DUNKERTON,^e
SHINGO WATANABE,^a AND KAZUYOSHI KIKUCHI^b

^aJapan Agency for Marine-Earth Science and Technology, Yokohama, Japan

^bInternational Pacific Research Center, University of Hawai'i at Mānoa, Honolulu, Hawaii

^cDepartment of Atmospheric Sciences, University of Hawai'i at Mānoa, Honolulu, Hawaii

^dGraduate School of Science, The University of Tokyo, Tokyo, Japan

^eNorthwest Research Associates, Redmond, Washington

(Manuscript received 13 June 2019, in final form 6 September 2019)


ABSTRACT

Observational studies have shown that, on average, the quasi-biennial oscillation (QBO) exhibits a faster phase progression and shorter period during El Niño than during La Niña. Here, the possible mechanism of QBO modulation associated with ENSO is investigated using the MIROC-AGCM with T106 (~1.125°) horizontal resolution. The MIROC-AGCM simulates QBO-like oscillations without any nonorographic gravity wave parameterizations. A 100-yr integration was conducted during which annually repeating sea surface temperatures based on the composite observed El Niño conditions were imposed. A similar 100-yr La Niña integration was also conducted. The MIROC-AGCM simulates realistic differences between El Niño and La Niña, notably shorter QBO periods, a weaker Walker circulation, and more equatorial precipitation during El Niño than during La Niña. Near the equator, vertical wave fluxes of zonal momentum in the uppermost troposphere are larger and the stratospheric QBO forcing due to interaction of the mean flow with resolved gravity waves (particularly for zonal wavenumber ≥ 43) is much larger during El Niño. The tropical upwelling associated with the Brewer–Dobson circulation is also stronger in the El Niño simulation. The effects of the enhanced tropical upwelling during El Niño are evidently overcome by enhanced wave driving, resulting in the shorter QBO period. The integrations were repeated with another model version (MIROC-ECM with T42 horizontal resolution) that employs a parameterization of nonorographic gravity waves in order to simulate a QBO. In the MIROC-ECM the average QBO periods are nearly identical in the El Niño and La Niña simulations.

1. Introduction

The stratospheric quasi-biennial oscillation (QBO) is a quasi-periodic oscillation of the equatorial zonal wind between easterlies and westerlies with mean period of about 28 months. The QBO winds affect the meridional propagation of extratropical planetary waves, resulting in a dependence of average Northern Hemisphere polar night jet strength on the phase of the QBO (Holton and Tan 1980; Dunkerton and Baldwin 1991). The QBO modulation of the polar night jet is, on

average, accompanied by patterns of sea level pressure change at high latitudes and the distribution of mid-latitude storm tracks (Baldwin et al. 2001; Kidston et al. 2015; Gray et al. 2018). The stratospheric QBO also appears to affect weather in the tropical troposphere, as studies have related the patterns of tropical deep convection to the QBO phase (Collimore et al. 2003; Liess and Geller 2012). Chemical constituents such as ozone and water vapor are also affected by circulation changes associated with the QBO (Baldwin et al. 2001 and references therein). Recently publications have also connected the behavior of the Madden–Julian Oscillation (MJO) to the QBO phase. Notably evidence has been presented that the MJO is more active in the easterly phase than in the westerly phase of the QBO, and that the subseasonal predictability of the MJO is higher during the easterly phase than the westerly

 Denotes content that is immediately available upon publication as open access.

Corresponding author: Yoshio Kawatani, yoskawatani@jamstec.go.jp

DOI: 10.1175/JAS-D-19-0163.1

© 2019 American Meteorological Society. For information regarding reuse of this content and general copyright information, consult the [AMS Copyright Policy](#) (www.ametsoc.org/PUBSReuseLicenses).

phase (Yoo and Son 2016; Marshall et al. 2017; Nishimoto and Yoden 2017). Overall there is strong evidence that the QBO induces troposphere–stratosphere coupling and affects both dynamical and chemical processes over a wide meridional range.

The QBO is believed to be largely forced by atmospheric waves generated by tropical cumulus convection, and it seems likely that a broad spectrum of waves ranging from relatively small-scale inertia–gravity waves (GWs) to planetary-scale equatorial waves contribute significantly (Baldwin et al. 2001). More specifically, evidence suggests that the westerly acceleration phase of the QBO is forced by large-scale Kelvin waves and inertia–gravity waves (GWs) with a range of horizontal scales, while the QBO easterly mean accelerations are mainly driven by small-scale GWs (Hamilton et al. 1999; Kawatani et al. 2010a,b; Evan et al. 2012). Climate models with modest horizontal and vertical resolutions have generally not been able to simulate the QBO without a representation of the effects of subgrid-scale nonorographic gravity waves via a GW parameterization (GWP). Various in situ and remote sensing techniques currently allow some aspects of the GW field in the tropical stratosphere to be observed, but these are inadequate to determine the full global distribution and temporal variations of gravity waves and their sources (e.g., Alexander et al. 2010). Nonorographic GWPs have thus been developed based on generally oversimplified physical assumptions such as gravity wave sources and/or launch levels held constant in space and time.

While the QBO in the equatorial stratospheric zonal wind is notable for usually having a fairly repeatable evolution through each cycle, there are some quite apparent variations in the period and amplitude from cycle-to-cycle. The nature of this cycle-to-cycle variability is still not completely understood, but possible mechanisms that have been advanced include the interaction with annual cycle (leading to a tendency for the QBO to sometimes approach a state nearly locked onto 2- or 3-yr periods: Dunkerton 2017), effects of the solar cycle, effects of major volcanic eruptions and the effects of long-term forced climate change. Given the large effect of the El Niño–Southern Oscillation (ENSO) cycle on tropical convection, it is reasonable to suppose that ENSO may have a role in modulating QBO behavior. This idea has been considered since at least the early papers of Maruyama and Tsuneoka (1988) and Geller et al. (1997), and was given strong support from the more recent work of Taguchi (2010) who analyzed radiosonde observations of zonal wind from 70 to 10 hPa over Singapore (1.3°N) during the period 1953–2008. Taguchi reported that, on average, the QBO signals exhibit faster phase propagation during El Niño than

during La Niña conditions, and the amplitude of the QBO is weaker during El Niño. Yuan et al. (2014) largely confirmed these results in their analysis of radiosonde data from 10 near-equatorial stations, although they found that the ENSO influence on the QBO amplitude appears to be less robust than the ENSO influence on the QBO period.

As first shown in the classic works of Lindzen and Holton (1968) and Holton and Lindzen (1972), the interaction of dissipating, vertically propagating waves with the mean flow in the stratosphere should produce shear zones that exhibit apparent downward propagation. In the real atmosphere this effect should be opposed (and hence slowed) by the large-scale mean upwelling we expect near the equator in the stratosphere. We expect that, by itself, increased upwelling would slow the downward QBO phase propagation and hence lengthen the QBO period (Dunkerton 1997). Previous research has indicated that tropical upwelling is stronger during El Niño (Randel et al. 2009; Calvo et al. 2010; Simpson et al. 2011). Thus the shorter QBO periods during El Niño found by Taguchi (2010) must presumably be explained by an increased wave driving of the mean-flow accelerations, a point that Taguchi (2010) makes as well.

Schirber (2015) conducted a global model study of the ENSO modulation of the QBO. Specifically, he used the general circulation model (GCM) ECHAM6 (Stevens et al. 2013) which has a GWP in which the wave sources are assumed to depend on the strength of the model simulated moist convection as well as the mean winds in the source region (Beres et al. 2004). Schirber constructed two ensembles of different QBO initial conditions, with the onset of a westerly or easterly jet at 10 hPa, and integrated the model for 18 months for El Niño conditions and then for La Niña conditions. The parameterized GW mean momentum source in his experiment turned out to be ~15% larger in the El Niño run than in the La Niña run (refer to their Fig. 4), due to the El Niño induced increased precipitation and convective heating. Schirber found that the simulated QBO period is shorter in his El Niño runs than in his La Niña runs, and that the increased wave driving in the El Niño runs was found for both the resolved and parameterized waves. A momentum budget analysis indicated that the main driver of Schirber's simulated QBO is the parameterized gravity wave forcing, especially in the easterly acceleration phase. Note that a discussion of ENSO effects on the QBO is included in the recent review article of Domeisen et al. (2019).

The observed systematic ENSO effects on the QBO present a useful “yard stick” for evaluating comprehensive model simulations. Such evaluation may provide some degree of confidence in the ability of models

to simulate in a realistic manner the dynamics of the stratospheric QBO and its response to external forcing. An accurate simulation of the QBO–ENSO connection would also be valuable for models used in practical seasonal, and even further extended-range, weather forecasts (see [Boer and Hamilton 2008](#); [Scaife et al. 2014](#)). Given the QBO teleconnections with tropospheric circulation, practical extended-range weather forecasts will be improved with accurate representation of ENSO, the stratospheric QBO and the ENSO–QBO connection.

In the present study, we investigate possible mechanisms of ENSO modulation of the QBO using two global atmospheric models developed under the Model for Interdisciplinary Research on Climate (MIROC) framework. One model used is the MIROC-Atmospheric General Circulation Model (MIROC-AGCM) version employed in the earlier study of [Kawatani et al. \(2011\)](#). It is notable that sufficiently fine-vertical-resolution versions of the MIROC-AGCM simulate a fairly realistic tropical stratospheric QBO ([Kawatani et al. 2009, 2010a,b, 2011, 2014, 2019](#)). Here, we set a vertical resolution of 550 m from the upper troposphere to the stratosphere and a horizontal resolution of ~ 120 km (T106). No nonorographic GWP is included; thus, the simulated QBO is driven by only the resolved waves. The second model used here is the atmospheric part of the Model for Interdisciplinary Research on Climate, Earth System Model (MIROC-ESM; [Watanabe et al. 2011](#)) with a stratospheric vertical resolution of 700 m and a horizontal resolution of ~ 312 km (T42). In contrast with the MIROC-AGCM, the MIROC-ESM does include a Hines-type nonorographic GWP ([Hines 1997](#)), which is crucial to the simulation of a mean-flow QBO in this model ([Watanabe and Kawatani 2012](#)).

Rather than performing an ensemble of relatively short integrations (as in [Schirber 2015](#)) our study employed century-long continuous model integrations with annually repeating prescribed SSTs appropriate for typical El Niño and La Niña conditions. While the SST evolution experienced by the atmospheric model in this case is unrealistic in some respects (e.g., the SST field appropriate for the mature phase of an El Niño at the end of each calendar year is effectively followed by the developing phase of another El Niño in the first months of the following year), this simple design naturally produces a broad sampling of QBO phases relative to the annual cycle (although we acknowledge a limitation in that in the real world El Niño's and La Niña's begin or fade at various times of year). By basing our prescribed SST anomalies on composites of large numbers of actual historical months we can construct observed composites for various atmospheric fields that can be used for

comparison with our model's perpetual El Niño and La Niña runs.

This paper is arranged as follows. [Section 2](#) describes the models and the experimental design. [Section 3](#) describes the ENSO modulation of the QBO and climatological differences in the mean fields in the MIROC-AGCM experiments. [Section 4](#) investigates wave forcing differences between El Niño and La Niña in the MIROC-AGCM. [Section 5](#) discusses the ENSO modulation of the QBO in the MIROC-ESM with fixed parameterized gravity wave sources. [Section 6](#) summarizes the study and provides the conclusions.

2. Model description and experimental design

We use the same MIROC-AGCM model as in [Kawatani et al. \(2011\)](#). This version of the atmospheric part of the MIROC3.2 ([Hasumi and Emori 2004](#)) model (MIROC-AGCM) has a horizontal resolution of T106 spectral truncation, which corresponds to a grid interval of approximately 120 km in the tropics (1.125°). A total of 72 vertical numerical levels are used (L72) with the top boundary at 1.2 hPa (~ 47 km). The vertical resolution is close to 550 m from ~ 300 to 5 hPa, which should assist with adequate representation of the mean-flow interaction with vertically propagating waves ([Kawatani et al. 2019](#)). Above 4.5 hPa, the model includes artificial damping in a “sponge layer.” The [McFarlane \(1987\)](#) orographic GWP is employed, but no parameterization of nonorographic gravity wave effects is included. Hence, the simulated QBO is driven by explicitly resolved waves in the model. After a spinup period in each case the model was integrated continuously for 100 years for each of El Niño and La Niña cases.

The prescribed SST anomalies used in our El Niño case were functions of time of year and were computed from the AMIP SST data during 1950–2012 as the composite anomaly for each calendar month over all the months in the record classed as being in El Niño conditions. The same procedure was used to construct our annually repeating La Niña SST anomalies. In the construction of the composite SST patterns, the characterization of the ENSO state followed that of the Japan Meteorological Agency (JMA). The JMA data and data description are provided on the agency website (http://ds.data.jma.go.jp/tcc/tcc/products/el_nino/index.html).

The JMA definition of El Niño (La Niña) is such that the 5-month running-mean SST deviation for Niño-3 (5°S – 5°N , 150° – 90°W) continues at 0.5°C (-0.5°C) or higher (lower) for 6 consecutive months or longer. The Niño-3 SST deviations are calculated by the monthly mean SST in Niño-3 minus the monthly mean SST

TABLE 1. Number of El Niño and La Niña months during 1950–2012 based on data from the Japan Meteorological Agency. The max and min rows indicate the maximum Niño-3 anomalies (K) for El Niño and minimum anomalies for La Niña, respectively.

	Jan	Feb	Mar	Apr	May	Jun	Jul	Aug	Sep	Oct	Nov	Dec
El Niño month	15	13	9	11	13	16	16	15	16	16	16	15
Max	3.2	2.6	2.1	1.8	2.1	2.0	2.5	2.9	3.0	3.3	3.6	3.5
La Niña month	16	15	13	14	12	12	15	15	16	16	16	16
Min	−1.8	−1.5	−1.0	−1.3	−1.4	−2.0	−1.6	−1.6	−1.3	−1.6	−1.7	−1.8

climatological reference based on the latest sliding 30-yr period (see more details on the JMA website).

The El Niño and La Niña months are selected individually for each calendar month (i.e., each January, February, . . . , December) following the definition of the JMA. Monthly SST data are weighted by the values of the Niño-3 SST deviation and are then averaged.

As an example, we show here the procedure to create our composite January El Niño SST anomaly. El Niño in January occurred in the 15 years including 1952, 1958, 1964, 1966, 1969, 1970, 1973, 1977, 1983, 1987, 1988, 1992, 1998, 2003, and 2010 [referred to as SST(year)], with a Niño-3 SST deviation of Niño-3 0.8, 1.5, 0.7, 1.3, 0.7, 1.0, 2.0, 1.1, 3.0, 1.2, 0.5, 1.5, 3.2, 0.8, and 1.1 [referred to as Niño-3(year)]. Our composite January El Niño SST at any grid point, $\overline{\text{SST}}(\text{lon}, \text{lat})$ where lon and lat represent longitude and latitude, respectively, is then calculated from the 15 individual January SSTs weighted by the Niño-3 anomaly as follows:

$$\overline{\text{SST}}(\text{lon}, \text{lat}) = \frac{\sum \text{SST}(\text{lon}, \text{lat}, \text{year}) \times \text{NINO.3}(\text{year})}{\sum \text{NINO.3}(\text{year})}. \quad (1)$$

Table 1 shows the number of El Niño and La Niña months during a 63-yr period (1950–2012), with maximum and minimum Niño-3 temperature anomalies for the El Niño and La Niña months, respectively. January has 15 El Niño out of 63 months, with a maximum anomaly of 3.2 K (in 1998, see the JMA website). The calculated composite SST anomaly for the Niño-3 region in January is 1.92 K, and corresponds to a “moderately strong” El Niño.

Figures 1a and 1b show our annual-mean composite SST deviations from the climatology for El Niño and La Niña, and Figs. 1c and 1d show the composite Niño-3 SST anomalies through the year for El Niño and La Niña, respectively. To see the annual cycle easily we display a 2-yr period (just repeating the same composite values). The El Niño anomalies are smaller in the boreal summer and become larger in the boreal winter. Note that the procedure we applied is not able to fully represent the development, mature phase, and decay of all observed El Niño events since the evolution of an event may occur over a period longer than 1 year. However,

the shape of the time evolution is similar to that seen in real events, insofar as El Niño amplitudes tend to peak during the boreal winter. On the other hand, La Niña shows no clear standard seasonal development, and the evolution of SST anomalies varies considerably among individual La Niña events.

The monthly El Niño and La Niña SSTs used in our model integrations are obtained by adding the composite monthly SST anomaly to the monthly climatological SSTs averaged from 1979 to 1998, respectively. Only the imposed SSTs differ between our El Niño and La Niña runs, and other prescribed fields, such as the sea ice and stratospheric ozone distributions, are the same.

In this study, we have also conducted the same ENSO–QBO experiments using the atmospheric component of MIROC-ESM (referred to simply as the MIROC-ESM after this). The horizontal resolution for this model is T42, and there are 80 layers from the surface to 85 km height (T42L80). The vertical resolution in the stratosphere is ~ 700 m. The Hines-type nonorographic GWP with fixed wave sources is used (Hines 1997). In MIROC-ESM, the QBO is spontaneously generated via the combination of explicitly resolved wave forcing and parameterized gravity wave forcing (Watanabe and Kawatani 2012).

3. The ENSO modulation of the QBO and climatological differences in the mean fields in the MIROC-AGCM

Figure 2 shows a time–height cross section of the monthly and zonal-mean zonal winds over the equator in the El Niño and La Niña runs with the MIROC-AGCM. The red and blue colors correspond to westerlies and easterlies, respectively. For simplicity, only results from the first 20 postspinup years in each experiment are shown here. In both runs, an obvious QBO-like oscillation is simulated. Westerly phases in the El Niño run sometimes penetrate to ~ 90 hPa, while they stop around ~ 70 hPa in the La Niña run. Notably the westerly to easterly phase transitions around 30–50 hPa in the La Niña run display slower downward progression.

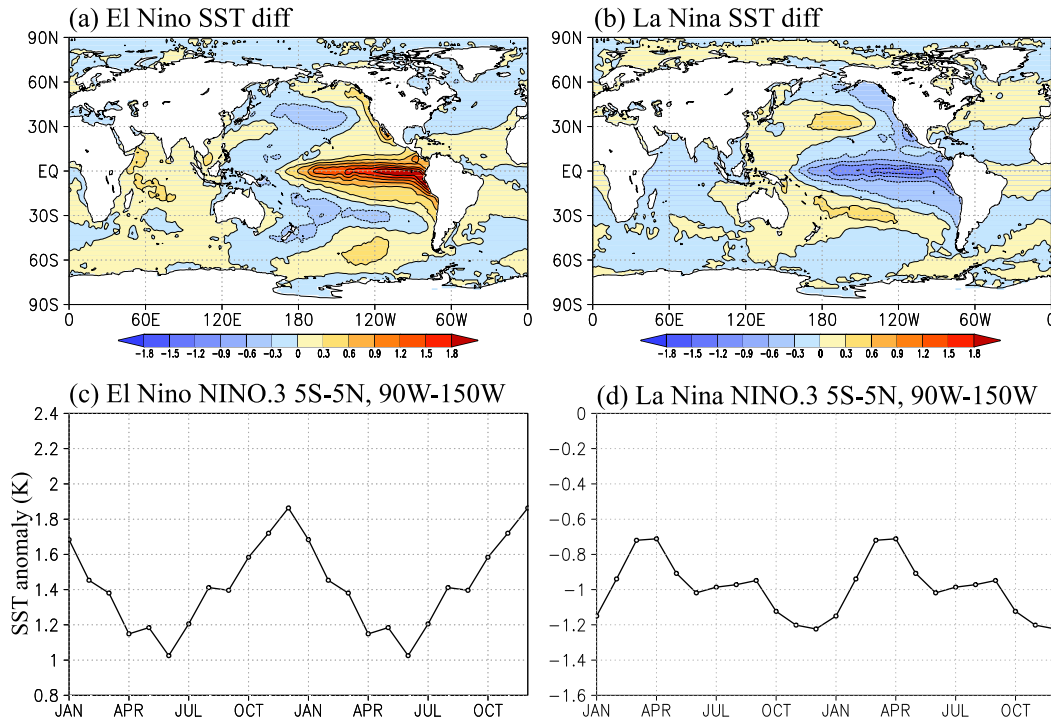


FIG. 1. (top) Annual-mean composite SST deviations from climatology for (a) El Niño and (b) La Niña. The color interval is 0.3 K. (bottom) The time variation of the monthly mean composite Niño-3 SST deviation from climatology for (c) El Niño and (d) La Niña. For visualization, two full repeating cycles are shown.

Figure 3 presents the analysis of the periods of individual QBO cycles in the El Niño and La Niña runs for the entire 100-yr integrations. For each simulated cycle a period with an integral number of months is computed

from the first month, during which the monthly and zonal-mean zonal winds at 20 hPa change from westerly to easterly, to the last month, defined as 1 month before the next transition at 20 hPa. The QBO periods vary

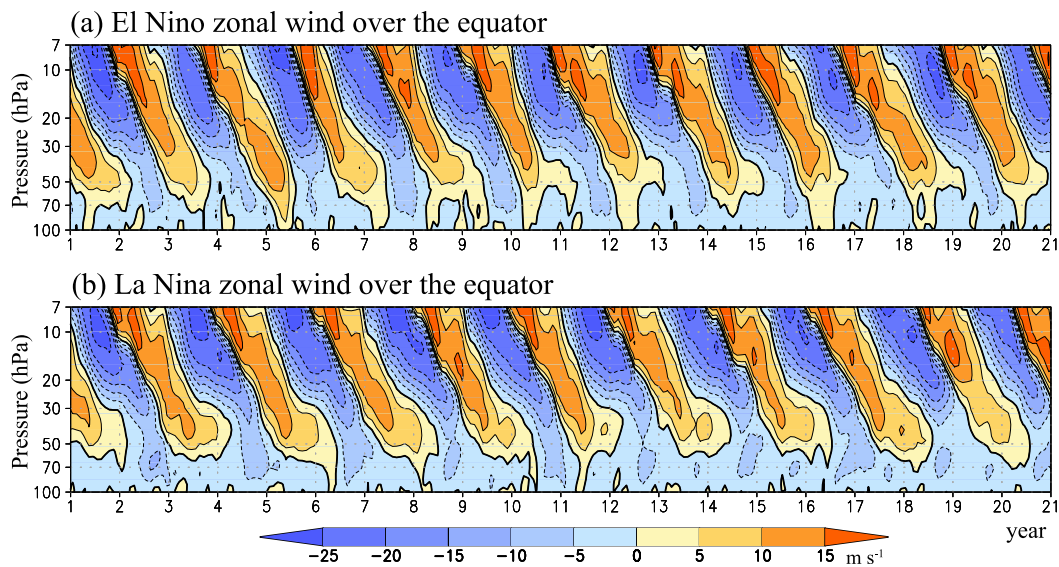


FIG. 2. Time–height cross sections of the monthly and zonal-mean zonal wind over the equator in the (a) El Niño and (b) La Niña runs with the MIROC-AGCM. The color interval is 5 m s⁻¹.

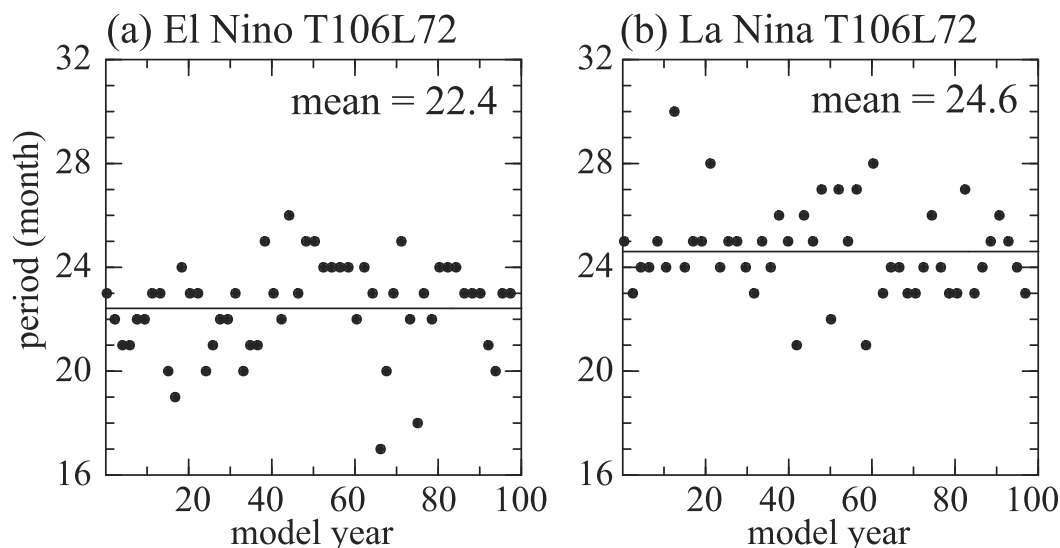


FIG. 3. Time series of the QBO periods in the 100-yr (a) El Niño and (b) La Niña runs with the MIROC-AGCM. Solid lines show the mean QBO periods for El Niño (22.4 months) and La Niña (24.6 months). Differences in the QBO period between El Niño and La Niña have statistical confidence levels $\geq 99\%$.

from 17 to 26 months for El Niño and 21 to 30 months for La Niña. Solid lines show mean QBO periods: 22.4 months for El Niño and 24.6 months for La Niña. Differences in the mean QBO period between the two experiments are about 2.2 months which differs from zero with a statistical confidence of $\geq 99\%$. The analysis of the observed near-equatorial winds by [Yuan et al. \(2014\)](#) arrived at long-term means for the QBO period of 25 months for El Niño conditions and 31.8 months for La Niña conditions.

Next, the QBO amplitude is investigated. Following [Dunkerton and Delisi \(1985\)](#), at each level we first calculate the standard deviation σ_u of the monthly mean time series after the mean seasonal cycle has been removed and then estimate the amplitude as $\sqrt{2}\sigma_u$ (this assumes that almost all the interannual variability in the monthly means in the equatorial stratosphere can reasonably be attributed to the QBO).

[Figure 4](#) shows vertical profiles of the QBO mean amplitude over the equator in El Niño and La Niña, and [Fig. 4b](#) depicts the ratios of the amplitudes between El Niño and La Niña (El Niño divided by La Niña). The QBO amplitude in El Niño is larger in the lowermost (100–65 hPa) and middle (~45–17 hPa) altitudes than in La Niña, whereas the La Niña amplitude is larger above ~15 hPa and ~50 hPa. The percentage differences are largest in the lowermost stratosphere and around 30 hPa (up to 20%); the largest absolute difference is only 1.7 m s^{-1} and occurs at 25 hPa.

Now we will discuss the climatological annual-mean differences in various fields between the El Niño and

La Niña runs, with a focus on those regions where the differences are judged to be significant at greater than 95% confidence. The statistical confidence estimates are based on the two-sided Student's t test for sampling the 100 individual yearly mean data for each of the El Niño and La Niña runs. For comparison, observational estimates from ERA-Interim (ERA-I) and the CPC Merged Analysis of Precipitation (CMAP; [Xie and Arkin 1997](#)) precipitation dataset are used. The computation of the observed El Niño and La Niña composites for each calendar month proceeded as for the SST composites discussed in [section 2](#), but using reanalysis data (or gridded rainfall data in [Fig. 6](#)) restricted to 1979–2012. The observed El Niño minus La Niña results shown below in [Figs. 5–7](#) are computed from annual means of these composites.

[Figures 5a and 5b](#) show longitude–height cross sections of the climatological annual-mean zonal wind for the El Niño and La Niña runs at 10°N – 10°S . The Walker circulation is obviously different between El Niño and La Niña. Both the easterlies in the Eastern Hemisphere and the westerlies in the Western Hemisphere are larger in La Niña than in El Niño. Since the Walker circulation filters gravity waves propagating from the troposphere to the stratosphere, a weaker Walker circulation during El Niño could result in more gravity wave propagation into the stratosphere due to less filtering of gravity waves (e.g., [Figs. 6 and 7](#) of [Kawatani et al. 2010b](#)). This argument assumes critical-level absorption of otherwise weakly damped, vertically propagating waves, similar to the ideal model of [Lindzen and Holton \(1968\)](#).

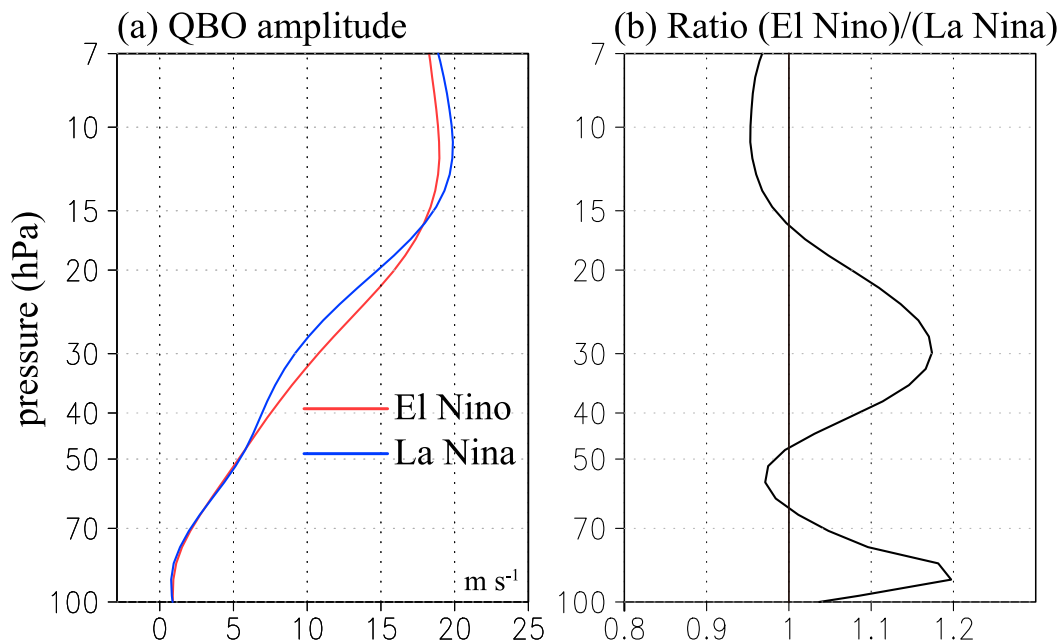


FIG. 4. (a) Vertical profiles of the QBO amplitude over the equator (m s^{-1}) in the MIROC-AGCM runs. The QBO amplitude for each individual cycle is calculated at each level based on the dates on which the zonal-mean zonal wind at 20 hPa changes from westerly to easterly. The mean QBO amplitude is averaged over 52 and 47 QBO cycles for the El Niño and La Niña simulations, respectively. (b) The vertical profile of the ratio of the QBO amplitude, El Niño divided by La Niña.

The El Niño minus La Niña differences in near-equatorial zonal wind are shown in Fig. 5c for the model and Fig. 5d for ERA-I. In the Pacific, around 120°E – 90°W , large easterly differences are found from ~ 500 to 80 hPa, and westerly differences are found both below and above the region with easterly differences. In other longitudes above ~ 500 hPa, westerly El Niño minus La Niña differences are seen, with small easterly differences in the lower troposphere. These patterns are very similar between the model and ERA-I. Around 50–90 hPa, weak westerly differences are found around in both ERA-I and the model, due to slightly weaker easterly in El Niño than La Niña.

Figures 6a and 6b show climatological annual-mean precipitation differences in El Niño minus La Niña for the CMAP observations and for the model. The simulated differences, such as more precipitation in the equatorial eastern Pacific and less precipitation around the maritime continents, are similar to those in CMAP, although the observed weaker precipitation to the northeast of the Philippines in El Niño is not captured in the model. Figure 6c depicts longitudinal variations in El Niño minus La Niña precipitation differences averaged over 10°N – 10°S , while Fig. 6d shows latitudinal variations in zonal-mean precipitation differences; again, results are shown for the CMAP observations and our

model integrations. The longitudinal variations in equatorial precipitation differences and latitudinal differences in the zonal-mean precipitation in the model are quite similar to those in CMAP. Zonal-mean precipitation over the equator in El Niño is $\sim 15\%$ larger than that in La Niña for both the CMAP observations and MIROC model.

Figure 7a shows the climatological annual- and zonal-mean temperature in El Niño (purple lines) and La Niña (green lines) periods, along with their El Niño minus La Niña differences computed from the ERA-I composites. Figure 7c shows the same quantities for the zonal-mean zonal wind and Figs. 7b and 7d present comparable analysis for our model integrations. At $\sim 30^{\circ}\text{S}$ – 30°N , in El Niño the troposphere is warmer and the stratosphere is cooler (cf. Domeisen et al. 2019) for both the model and ERA-I, although the model differences are spread somewhat wider meridionally. Cooler differences to the polar side of the warm difference region in the troposphere are also seen in both the model and ERA-I, and simulated warm differences in the mid- to high-latitude stratosphere are also similar to those in ERA-I. There are some discrepancies between the model and ERA-I, such as the tropospheric temperature anomalies having opposite signs around 60° – 90°N .

The model also captures the overall pattern of zonal-mean zonal wind differences seen in the observations

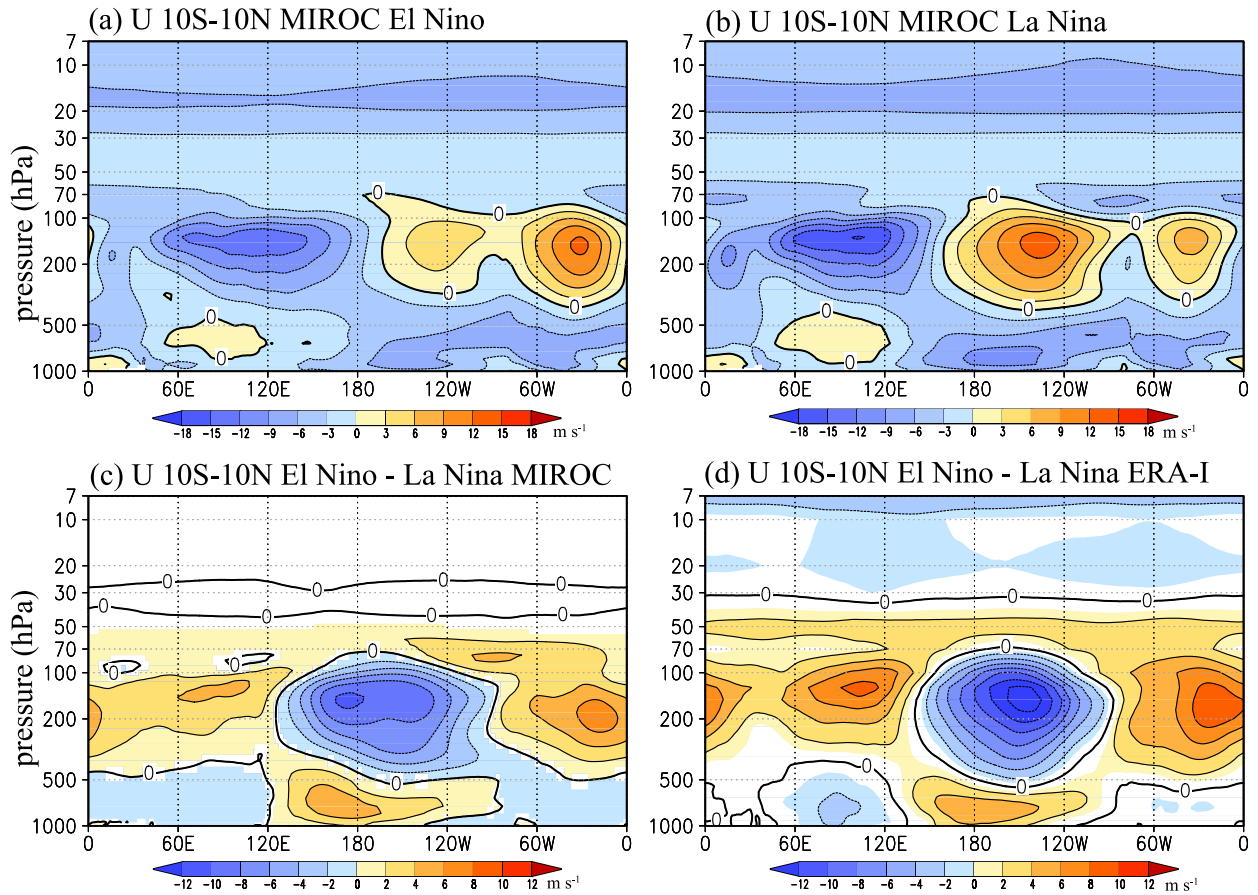


FIG. 5. (top) Longitude–height cross sections of the climatological annual-mean zonal wind during (a) El Niño and (b) La Niña averaged over 10°N–10°S. (bottom) Zonal wind differences in El Niño minus La Niña for (c) MIROC-AGCM and (d) ERA-I. Differences with a statistical confidence $\geq 95\%$ are shaded in (c), and those with absolute values $\geq 1 \text{ m s}^{-1}$ are shaded in (d).

(Figs. 7c,d). Over the equator, westerly differences around 900 hPa, easterly differences around 500–100 hPa, and westerly differences in the lowermost stratosphere are seen in both the model and ERA-I. Westerly differences are found from the lower troposphere to the stratosphere outside the equatorial region. Poleward of these regions of westerly differences, easterly differences are found from the surface to the stratosphere.

Different distributions of the background zonal-mean zonal wind could alter the wave propagation properties and thus modify the stratospheric Brewer–Dobson circulation (BDC). The westerly El Niño minus La Niña differences in the midlatitude lower stratosphere are somewhat similar to what is seen in global warming versus present day climate simulations (e.g., Kawatani et al. 2011).

To analyze the wave propagation and zonal wave forcing, the Eliassen–Palm flux (EP flux) in spherical and log-pressure coordinates is used (Andrews et al. 1987):

$$F^{(\phi)} = \rho_0 a \cos\phi (\bar{u}_z \bar{v}'\theta' / \bar{\theta}_z - \bar{u}'v'), \quad (2)$$

$$F^{(z)} = \rho_0 a \cos\phi \{ [f - (a \cos\phi)^{-1} (\bar{u} \cos\phi)_\phi] \times \bar{v}'\theta' / \bar{\theta}_z - \bar{u}'w' \}, \quad (3)$$

$$\nabla \cdot \mathbf{F} = (a \cos\phi)^{-1} \partial / \partial \phi [F^{(\phi)} \cos\phi] + \partial F^{(z)} / \partial z. \quad (4)$$

The zonally averaged momentum equation in terms of the transformed Eulerian mean (TEM) formulation is expressed as

$$\bar{u}_t = \bar{v}^* [f - (a \cos\phi)^{-1} (\bar{u} \cos\phi)_\phi] - \bar{w}^* \bar{u}_z + (\rho_0 a \cos\phi)^{-1} \nabla \cdot \mathbf{F} + \bar{X}. \quad (5)$$

In the above equations, ρ_0 , a , ϕ , z , u , v , w , θ , and f are the log-pressure height-dependent density, the mean radius of Earth, latitude, log-pressure height, zonal wind, meridional wind, vertical wind, potential temperature, and Coriolis parameter ($f \equiv 2\Omega \sin\phi$, where

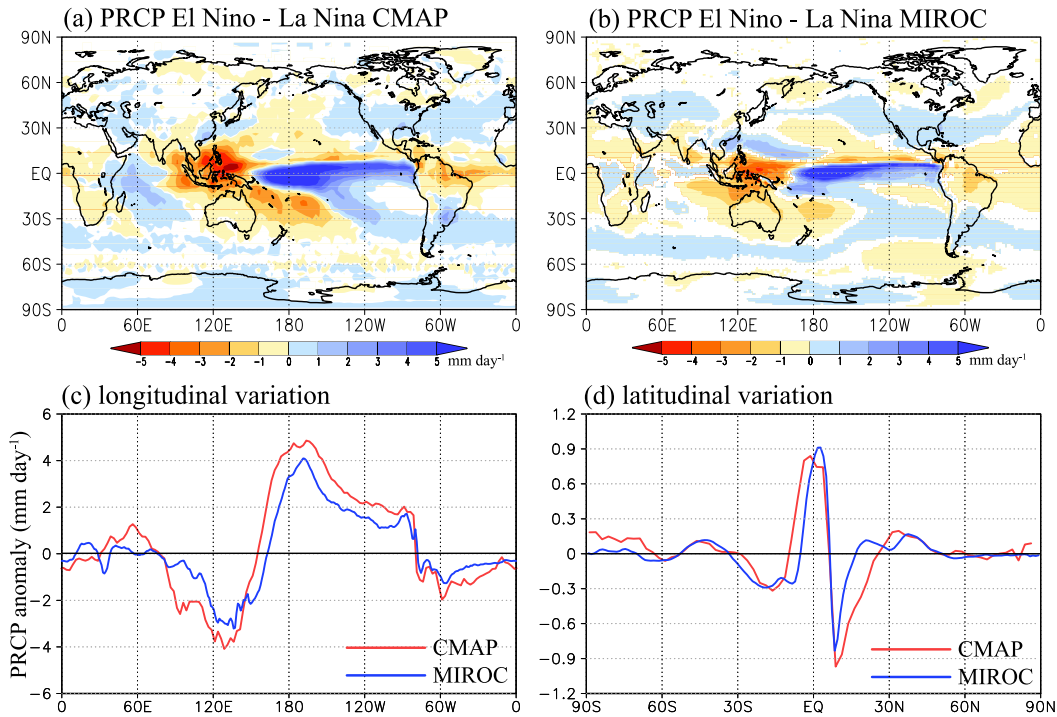


FIG. 6. Climatological annual-mean precipitation differences for El Niño minus La Niña for (a) CMAP and (b) MIROC-AGCM. Color interval is 1 mm day⁻¹. Differences with absolute values ≥ 0.1 mm day⁻¹ are shaded in (a), and those with a statistical confidences $\geq 95\%$ are shaded in (b). (c) Longitudinal variations of precipitation differences at 10°N–10°S and (d) latitudinal variations of zonal-mean precipitation differences for CMAP (red) and MIROC-AGCM (blue).

Ω is the rotation rate of Earth), respectively. The subscripts ϕ , z , and t denote the meridional, vertical, and time derivatives, respectively. The mean residual circulations of the meridional and vertical components are expressed by \bar{v}^* and \bar{w}^* . Eastward and westward wave forcing of the mean flow correspond to the EP-flux divergence and convergence (i.e., $\nabla \cdot \mathbf{F} > 0$ and $\nabla \cdot \mathbf{F} < 0$), respectively. Note that below we will use the term “EP-flux divergence” loosely to refer to the eddy contribution to the mean-flow acceleration [i.e., the third term on the right-hand side in Eq. (5)]. The \bar{X} term is unresolved forcing, such as forcing due to a GWP.

Figure 8a shows the climatological annual-mean EP flux and EP-flux divergence from explicitly resolved eddies of all scales in the El Niño model run, while Fig. 8b displays the zonal-mean-flow forcing due to parameterized orographic gravity waves also in the El Niño run. The contour lines represent the zonal-mean zonal wind. Positive and negative values of wave forcing correspond to eastward and westward mean-flow driving. Resolved waves with westward momentum propagate upward around 30°–70°N and 30°–70°S and equatorward in low latitudes (Fig. 8a). Equatorward propagation becomes very weak around the 0 m s⁻¹ lines of the zonal wind. Around 60°S and 60°N, resolved

waves propagate directly upward toward the upper stratosphere. On the other hand, there is large westward wave forcing due to orographic GWP in the midlatitude upper troposphere–lower stratosphere (UTLS) region in both hemispheres where the westerlies are weak (Fig. 8b). This forcing plays a substantial role in decelerating the upper part of the subtropical westerly jet.

Figure 8c shows the El Niño minus La Niña differences of the EP flux and its divergence. Large westward forcing anomalies are found at 5°–70°N and 5°–60°S around 30–100 hPa. The EP-flux differences indicate that more waves with westward momentum preferentially propagate into the lower stratosphere during El Niño. As a result, westward forcing differences lie above the eastward wave forcing in the UTLS off-equatorial region.

Figure 8d shows the El Niño minus La Niña forcing differences due to parameterized orographic gravity waves. Note El Niño minus La Niña differences of surface zonal winds over midlatitude mountains such as the Himalaya, Rocky, and Andes Mountains are small (not shown). Westward forcing differences due to the orographic GWP occur in the midlatitudes around 30–80 hPa in both the Northern and Southern Hemispheres, whereas eastward forcing anomalies are

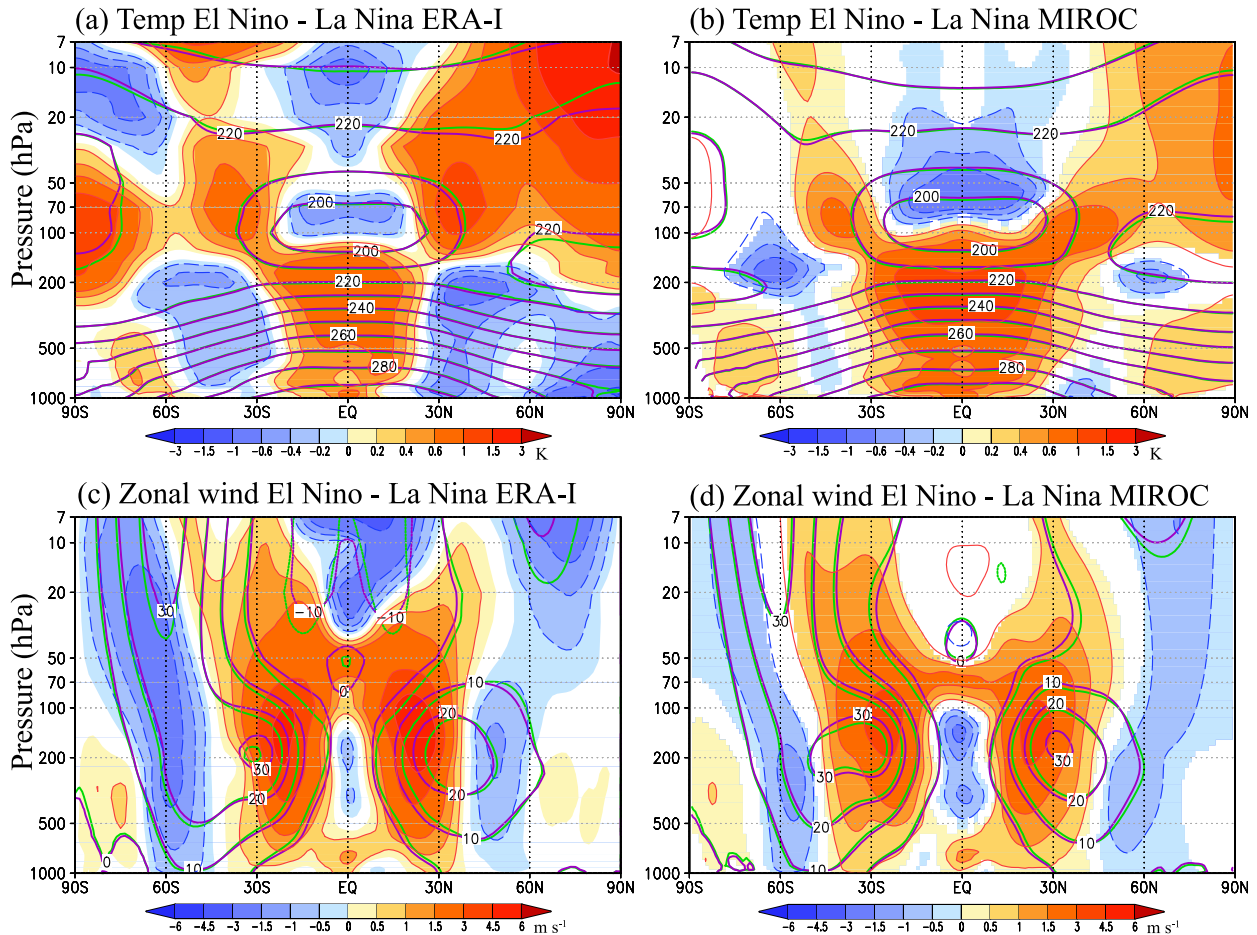


FIG. 7. Contour lines show the climatological annual- and zonal-mean (a),(b) temperature and (c),(d) zonal wind for El Niño (purple) and La Niña (green) for (a),(c) ERA-I and (b),(d) MIROC-AGCM. Contour intervals are 10 K for temperature and 10 m s^{-1} for zonal wind. Color shading indicates El Niño minus La Niña with absolute values ≥ 0.2 K and 0.1 m s^{-1} in (a) and (c) and those with statistical confidence $\geq 95\%$ in (b) and (d). Color intervals are $\pm 0.2, 0.4, 0.6, 1, 1.5,$ and 3 K for temperature and $\pm 0.5, 1, 1.5, 3, 4.5,$ and 6 m s^{-1} for zonal wind.

seen below the westward forcing anomalies, especially in the Northern Hemisphere (Fig. 8d). Given that the surface winds over the major midlatitude mountain regions change only very little between the El Niño and La Niña simulations, the change in the orographic GWP seen in Fig. 8d may be mainly due to changed mean-flow filtering. Shifting the zero line of the zonal wind (see purple and green lines in Fig. 7d) allows deeper penetration of the orographic waves and spreading the westward forcing from the waves to higher altitudes. This result is somewhat similar to that seen in global warming versus present day climate simulation (see Fig. 7 in Kawatani et al. 2011).

Figure 9a shows the climatological annual-mean residual streamfunction differences in El Niño minus La Niña runs. The residual mean circulation in El Niño appears to be strengthened with the differences in Fig. 9a generally corresponding to stronger upward and

poleward flow in the tropical stratosphere. As the wave forcing differences by both resolved and parameterized orographic gravity waves are primarily located in the midlatitude lower stratosphere, it is notably the shallow branch of the BDC that is seen to be intensified in the El Niño run.

To investigate quantitatively the mean ascent in the equatorial lower stratosphere, the residual vertical velocity in the TEM formation is calculated as follows (Andrews et al. 1987):

$$\bar{w}^* = \bar{w} + (a \cos \phi)^{-1} (\cos \phi \bar{v}' \theta' / \theta_z)_\phi. \quad (6)$$

Figure 9b shows the latitude–height cross section of the climatological annual-mean \bar{w}^* differences in El Niño minus La Niña. Corresponding to the residual streamfunction differences in Fig. 9a, tropical upwelling and mid- to high-latitude downwelling differences are seen

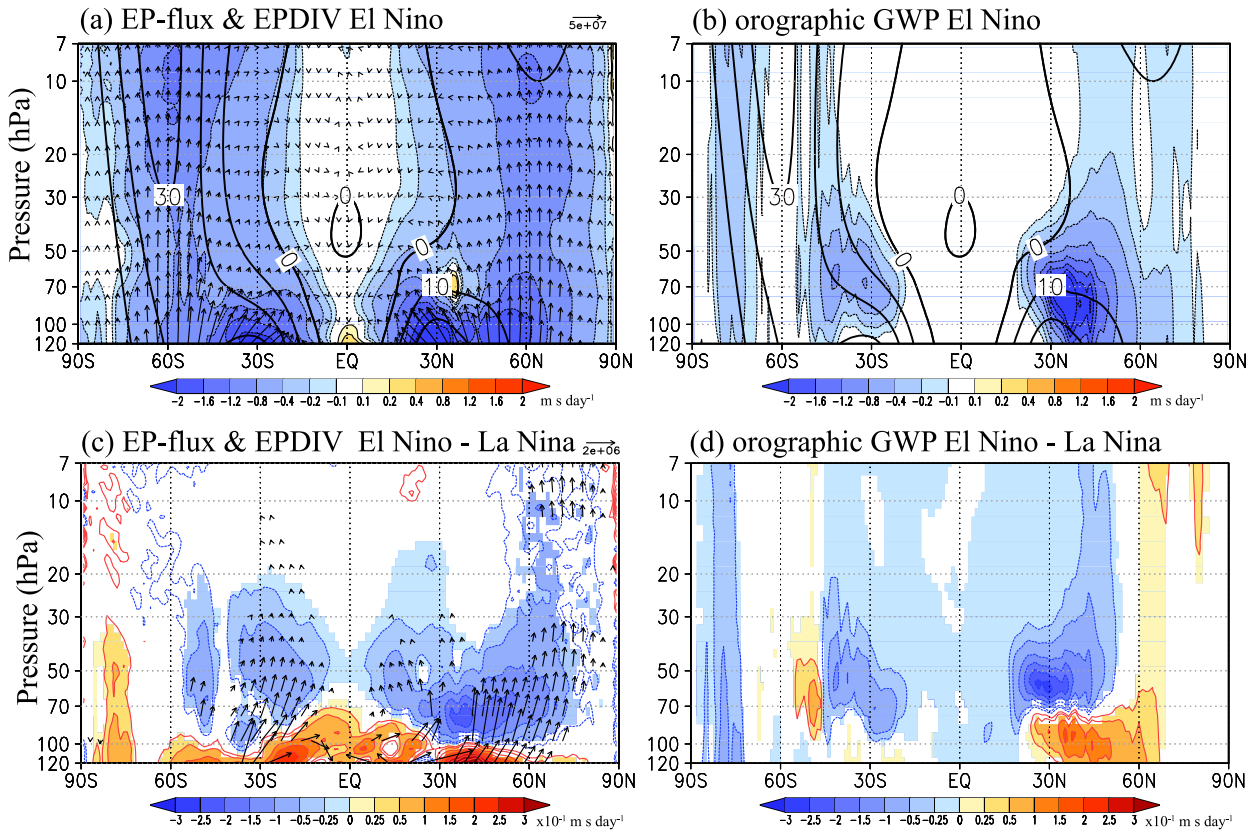


FIG. 8. (top) Climatological annual-mean (a) EP flux (vectors) and EP-flux divergence (colors) and (b) zonal forcing due to orographic GWP in the El Niño run. Zonal wind is contoured with intervals of 10 m s^{-1} . (bottom) Differences in El Niño minus La Niña of (c) the EP flux, its divergence and (d) parameterized wave forcing. The vertical components of the EP flux are multiplied by a factor of 660. Color intervals are at $\pm 0.1, \pm 0.2, \pm 0.4, \pm 0.8, \pm 1.2, \pm 1.6,$ and $\pm 2.0 \text{ m s}^{-1} \text{ day}^{-1}$ in (a) and (b) and $\pm 0.25, \pm 0.5, \pm 1.0, \pm 1.5, \pm 2.0, \pm 2.5,$ and $\pm 3.0 \text{ m s}^{-1} \text{ day}^{-1}$ in (c) and (d). The arrow units are $5.0 \times 10^7 \text{ kg s}^{-2}$ for (a) and $2.0 \times 10^6 \text{ kg s}^{-2}$ for (c). Differences in El Niño minus La Niña with statistical confidence levels $\geq 95\%$ are colored in (c) and (d).

in the \bar{w}^* field. Figure 9c shows the vertical profiles of ratios of El Niño \bar{w}^* to La Niña \bar{w}^* (i.e., El Niño divided by La Niña) averaged over $10^\circ\text{S}–10^\circ\text{N}$, $15^\circ\text{S}–15^\circ\text{N}$, and $20^\circ\text{S}–20^\circ\text{N}$. In the El Niño run, \bar{w}^* is strengthened by up to 24% for $10^\circ\text{S}–10^\circ\text{N}$, 21% for $15^\circ\text{S}–15^\circ\text{N}$, and 17% for $20^\circ\text{S}–20^\circ\text{N}$ around 50–70 hPa, while the ratio becomes closer to 1 or even less than 1 around $10^\circ\text{S}–10^\circ\text{N}$ in the middle to upper stratosphere. The mean equatorial upwelling is strengthened much more in the lower stratosphere than in the middle to upper stratosphere.

If the wave forcing relevant to the QBO does not change, \bar{w}^* could primarily determine the QBO period (Dunkerton 1997). By itself, the increase seen in equatorial \bar{w}^* in the El Niño run should lengthen the QBO period. The fact that we actually see that the QBO periods are significantly shorter in the El Niño run (Figs. 2 and 3 above) presumably implicates an ENSO dependence of the wave driving of the equatorial mean flow. In the next section we will examine the differences in the

waves and wave driving of the mean flow in the El Niño and La Niña MIROC-AGCM simulations.

4. Wave forcing differences between El Niño and La Niña in the MIROC-AGCM

In this section, differences in the wave forcing between El Niño and La Niña are investigated. We computed fields in a composite QBO cycle for each of our El Niño and La Niña runs. The composite was defined based on the phase of the zonal wind QBO. Month 0 of the composite is taken to be when the zonal-mean wind at 20 hPa in the deseasonalized and smoothed (5-month running-mean) zonal wind series changes from westerly to easterly. Composite values of the original unsmoothed data were then computed for ± 18 months around these 0 months. A total of 52 and 47 cycles from the 100-yr simulations are averaged for El Niño and La Niña runs, respectively.

Figure 10 shows the near-equatorial ($10^\circ\text{S}–10^\circ\text{N}$) results for composited zonal-mean zonal wind (thick black

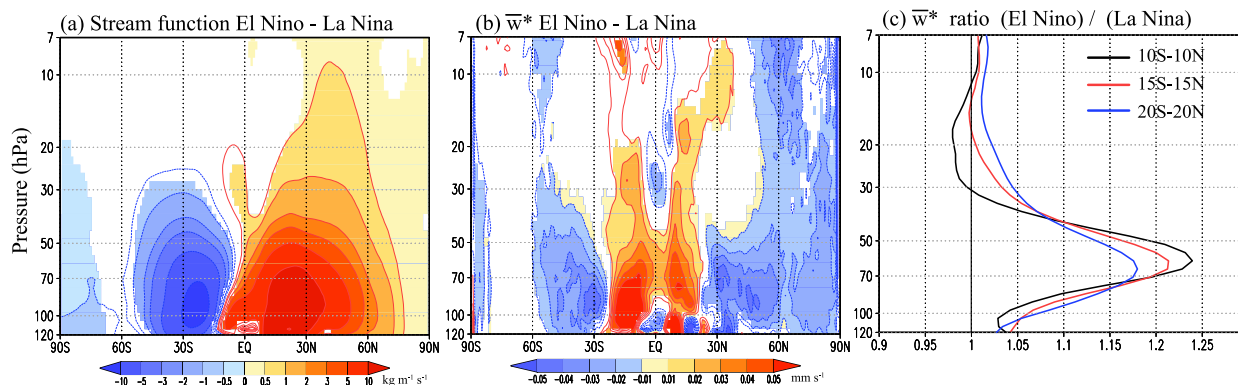


FIG. 9. Climatological annual-mean (a) residual streamfunction and (b) residual vertical velocity differences of El Niño minus La Niña runs. Differences with statistical significances of $\geq 95\%$ are colored. The color intervals are at 0, ± 0.5 , ± 1 , ± 2 , ± 3 , ± 5 , and $\pm 10 \text{ kg m}^{-1} \text{ s}^{-1}$ in (a) and 0.01 mm s^{-1} in (b). (c) Ratio of the El Niño to La Niña runs for the climatological residual vertical velocity averaged over 10°S – 10°N (black), 15°S – 15°N (red), and 20°S – 20°N (blue) as a function of height.

contours) and the EP flux convergence from explicitly resolved eddies (thin contours and shading). The delayed downward phase progression of the easterly regime around 30–50 hPa in La Niña relative to El Niño seen earlier in Fig. 2 is also clear in these composites (see the contour lines around 30–50 hPa during months 3–9 in Fig. 10). The westward forcing (corresponding to negative EP-flux divergence) around 40–70 hPa is larger in the El Niño simulation (see the $-0.05 \text{ m s}^{-1} \text{ day}^{-1}$ thin color contour).

Figure 11 shows the time variation of the zonal wind tendency \bar{u}_t [left-hand side in Eq. (5)], the EP-flux divergence (third term on the right-hand side), and forcing due to the residual circulation (first plus second term on the right-hand side) through the El Niño and La Niña QBO composites at 10, 20, and 40 hPa. Note that in our MIROC-AGCM simulations \bar{X} (fourth term on the right-hand side) is small in the equatorial region, as we do not use nonorographic GWP. The shorter QBO period in El Niño versus La Niña is evident in the composite. Owing to cycle-to-cycle variability entering the composite, there are minor differences in extrema between positive and negative lead times.

The period differences between El Niño and La Niña in this MIROC-AGCM experiment are only about 10% of the long-term-mean periods (see Fig. 3 above) so it is not surprising that only fairly modest differences are seen in the composite TEM momentum budget analyses in Fig. 11. However, the differences are quite systematic, so for example, the zonal wind tendency at 40 hPa is clearly weaker in La Niña both in the eastward (westerly) acceleration phase and the westward (easterly) acceleration phases, as seen during months -7 to -2 and months 2 to 7, respectively. Such differences are still found at 10 and 20 hPa (e.g., months 4–7 at 10 hPa), but they are more obvious at 40 hPa. El Niño versus La Niña

differences in wave forcing (red curves in the right-hand panels) are very obvious at 40 hPa during westward acceleration (negative values), but less so during eastward acceleration (positive values). Wave forcing and forcing due to advection by the residual circulation (blue curves) generally have opposite signs. At 40 hPa, differences in the wave forcing between El Niño and La Niña are larger than the differences in residual circulation forcing, especially during the westward acceleration phase (negative zonal wind tendency \bar{u}_t). These larger westward forcings in the El Niño run than in the La Niña run are found from ~ 40 to ~ 60 hPa (see the blue curve in Fig. 10). The effects of the mean momentum advection by the enhanced tropical upwelling associated the stronger BDC during El Niño are overcome by enhanced wave driving, resulting in a shorter period of the QBO.

Next, in order to investigate the contribution of different horizontal scales of resolved waves to the wave forcing differences between the El Niño and La Niña runs, the EP-flux divergences associated with zonal wavenumber (s) bands $1 \leq s \leq 11$, $12 \leq s \leq 42$, and $43 \leq s \leq 106$ were calculated. Figure 12 shows the time variation of the QBO composite zonal wave forcing due to each of these wavenumber bands at 10, 20, and 40 hPa. At 10 hPa, wave forcing due to each band is not very different between the El Niño and La Niña runs. At 20 hPa, some small differences, such as a larger eastward wave forcing due to $1 \leq s \leq 11$ and westward wave forcing due to $s \geq 43$ during El Niño, are seen. At 40 hPa, westward forcing is larger in all wave bands, but with particularly strong contribution from $43 \leq s \leq 106$ (Fig. 12i).

It is worth noting also the systematic differences that exist between eastward and westward wave forcings at 40 hPa, irrespective of ENSO [e.g., stronger westward

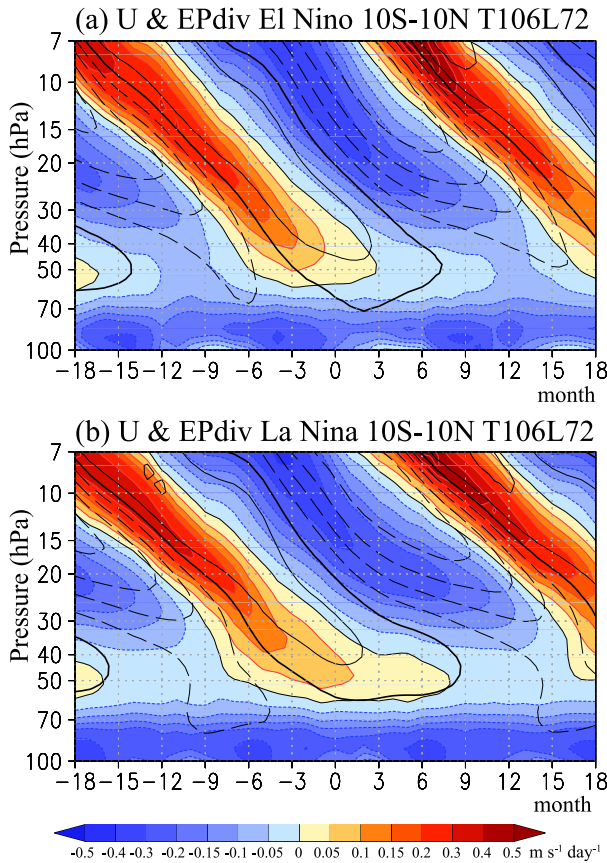


FIG. 10. Composite of the QBO 10°S–10°N zonal-mean zonal wind (contour lines) and EP-flux divergence (shading) for (a) El Niño and (b) La Niña runs with the MIROC-AGCM, where month 0 corresponds to the westerly to easterly phase transition of the zonal wind at 20 hPa. The contour line intervals are 5 m s⁻¹. The shading intervals are ±0.05, 0.1, 0.15, 0.2, 0.3, 0.4, and 0.5 m s⁻¹ day⁻¹.

forcing than eastward forcing due to $1 \leq s \leq 11$ waves (Fig. 12g) and stronger eastward forcing than westward forcing due to $12 \leq s \leq 42$ waves (Fig. 12h)]. These results are possibly affected by the simulated QBO amplitude. The present MIROC-AGCM with T106 resolution underestimates the QBO amplitude in the lower stratosphere. Kawatani et al. (2010a) indicated the T213 AGCM simulates a more realistic amplitude of the lower-stratospheric QBO than the T106 version (see their Fig. 1 and Fig. 9). Kawatani et al. showed similar time variation of monthly mean EP-flux divergence due to $1 \leq s \leq 11$, $12 \leq s \leq 42$, $43 \leq s \leq 106$ and $107 \leq s \leq 213$ in their Fig. 1 (only for one 3-yr realization). Eastward wave forcing due to $1 \leq s \leq 11$ and $12 \leq s \leq 42$ are nearly equal in their simulation. Underestimation of the lower-stratospheric QBO amplitude in the present T106 AGCM may contribute to such differences.

These analyses reveal that wave forcing of the mean flow from small-scale gravity waves (i.e., $43 \leq s \leq 106$)

likely contributes importantly to the QBO period differences between El Niño and La Niña (i.e., small-scale gravity waves contribute more to total wave forcing differences than do by larger-scale waves). As seen in Figs. 10–12, the differences are more obvious in the lower stratosphere than in the upper stratosphere. To clarify this height dependence of the wave forcing, we calculate the zonal wavenumber–frequency distribution of the vertical component of the EP flux $F^{(z)}$:

$$F^{(z)}(s, \omega) = \rho_0 a \cos \phi \operatorname{Re} \{ [f - (a \cos \phi)^{-1} (\bar{u} \cos \phi)] \times \hat{v}(s, \omega) \hat{\theta}^*(s, \omega) / \bar{\theta}_z - \hat{u}(s, \omega) \hat{w}^*(s, \omega) \}. \quad (7)$$

The asterisk denotes a complex conjugate, and \hat{u} , \hat{v} , \hat{w} , and $\hat{\theta}$ are the Fourier coefficients of the zonal, meridional, and vertical winds, and the potential temperature, respectively.

We selected pressure ranges of 123–114, 105–97, and 90–83 hPa for the analysis. El Niño minus La Niña differences in the climatological annual- and zonal-mean zonal wind over 10°S–10°N are slightly negative ($\sim -1 \text{ m s}^{-1}$) at 123–114 hPa, nearly zero at 105–97 hPa, and positive ($\sim 1.5 \text{ m s}^{-1}$) at 90–83 hPa (see Fig. 7d). Note that, for linear vertically propagating waves, the ground-based frequency ω and zonal wavenumber k are conserved in the vertical, assuming that the background flow does not change with time or longitude, respectively. The zonal wavenumber–frequency spectra of the EP fluxes will change with height in response to critical-level filtering and/or dissipation (Ern et al. 2008 and references therein). Therefore, the space–time spectra of $F^{(z)}$ at these altitudes, above filtering by the Walker circulation, are suitable for investigating how wave momentum fluxes relevant to the QBO differ between El Niño and La Niña runs. The spectra are calculated for successive overlapping segments of data and are then averaged. Herein, 72 days with 12 days of overlap between each segment are calculated (the total number of segments is 600 for 100 years).

Figure 13a shows the zonal wavenumber–frequency spectra of $F^{(z)}$ at 123–114 hPa between 10°S and 10°N averaged over all 100 years in the El Niño run. The solid lines depict the zonal phase velocity relative to the ground C_x . Positive zonal wavenumbers correspond to positive C_x values (eastward propagation), and negative zonal wavenumbers correspond to negative C_x values (westward propagation). $F^{(z)}$ is mostly distributed over a wide range of $|C_x|$ for both positive and negative zonal wavenumbers. Eastward-propagating waves transport the eastward momentum upward [i.e., negative $F^{(z)}$, corresponding to positive $\overline{u'w'}$; see Eq. (3)]. Note that

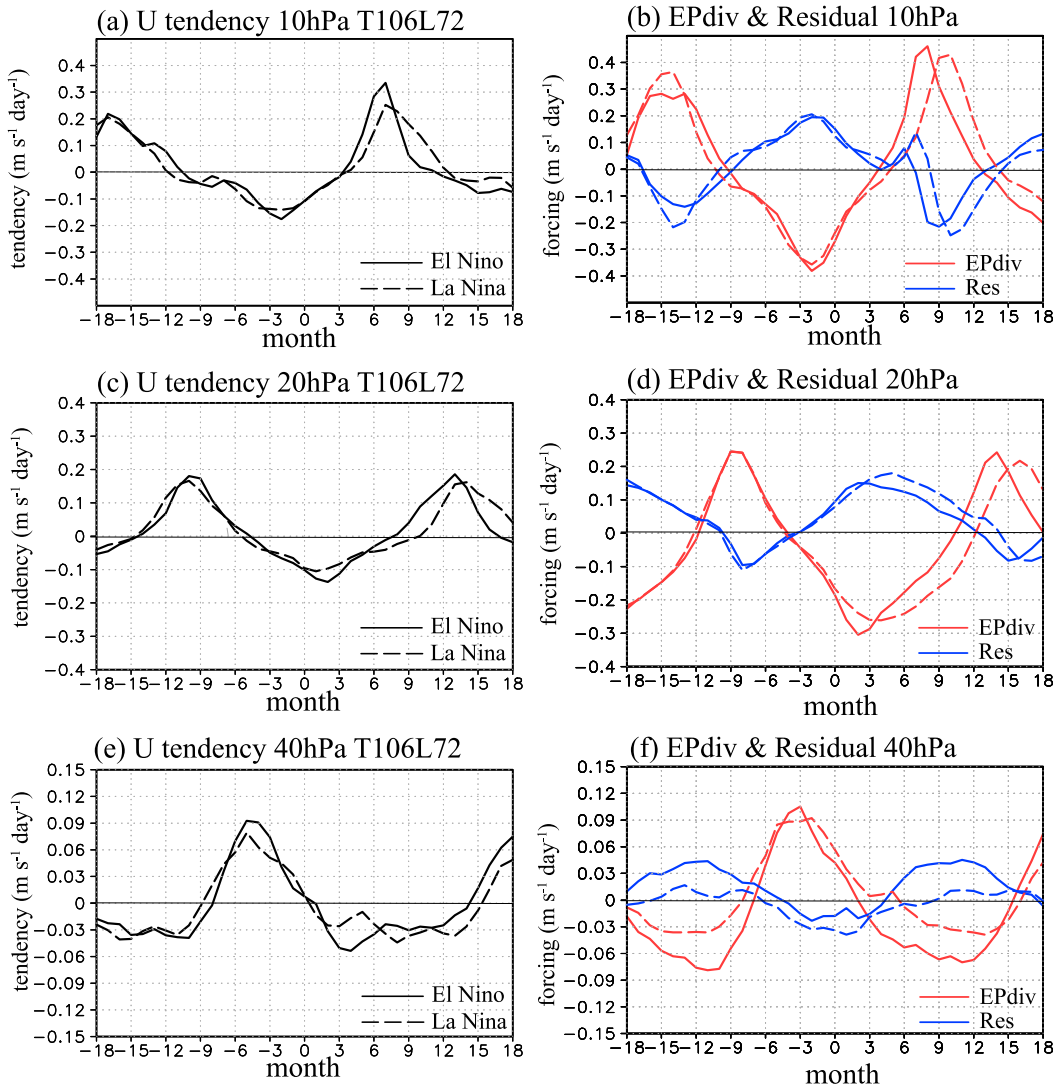


FIG. 11. Composite of the QBO in the (a),(c),(e) zonal wind tendency and (b),(d),(f) EP-flux divergence (red) and forcing due to the residual circulation (blue) at (a),(b) 10, (c),(d) 20, and (e),(f) 40 hPa averaged over 10°S – 10°N . Solid and dashed lines correspond to the El Niño and La Niña runs with the MIROC-AGCM, respectively.

the negative $F^{(z)}$ is colored red in Fig. 13a. Eastward momentum fluxes are seen for negative zonal wavenumbers with $-2 \leq C_x \leq 0 \text{ m s}^{-1}$ consistent with expectations of upward-propagating waves within a weak background mean easterly flow (-2 m s^{-1}).

Figures 13b–d show the $F^{(z)}$ El Niño-to-La Niña ratio for each spectral component. The 123–114-hPa layer is just above the ceiling for most deep convection (see Fig. 10 of Kawatani et al. 2011), and in this layer $|F^{(z)}|$ values are larger in El Niño than in La Niña for most spectral ranges. This is particularly so for $F^{(z)}$ with $|C_x| \leq 10 \text{ m s}^{-1}$. At 105–97 and 90–83 hPa, the $F^{(z)}$ ratio shows that there are much larger westward momentum fluxes in the El Niño run, especially those with $-10 < C_x < -2 \text{ m s}^{-1}$. On the

other hand, the $F^{(z)}$ ratio for $2 < C_x < 10 \text{ m s}^{-1}$ becomes smaller with the altitude increase. This is presumably due to more filtering of eastward- (westward-) propagating waves in El Niño (La Niña) above 90 hPa associated with westerly mean anomalies (Fig. 7d). Although mean westerly anomalies are small ($\sim 1.5 \text{ m s}^{-1}$), they may act to enhance the contrast between changes in vertical fluxes by eastward- and westward-propagating waves; consistent with larger westward forcing during El Niño than La Niña and to smaller differences of eastward forcing at 40 hPa (Figs. 11 and 12).

To study further the upward-propagating waves incident on the equatorial stratosphere, we investigate the space–time dependence of their convective wave

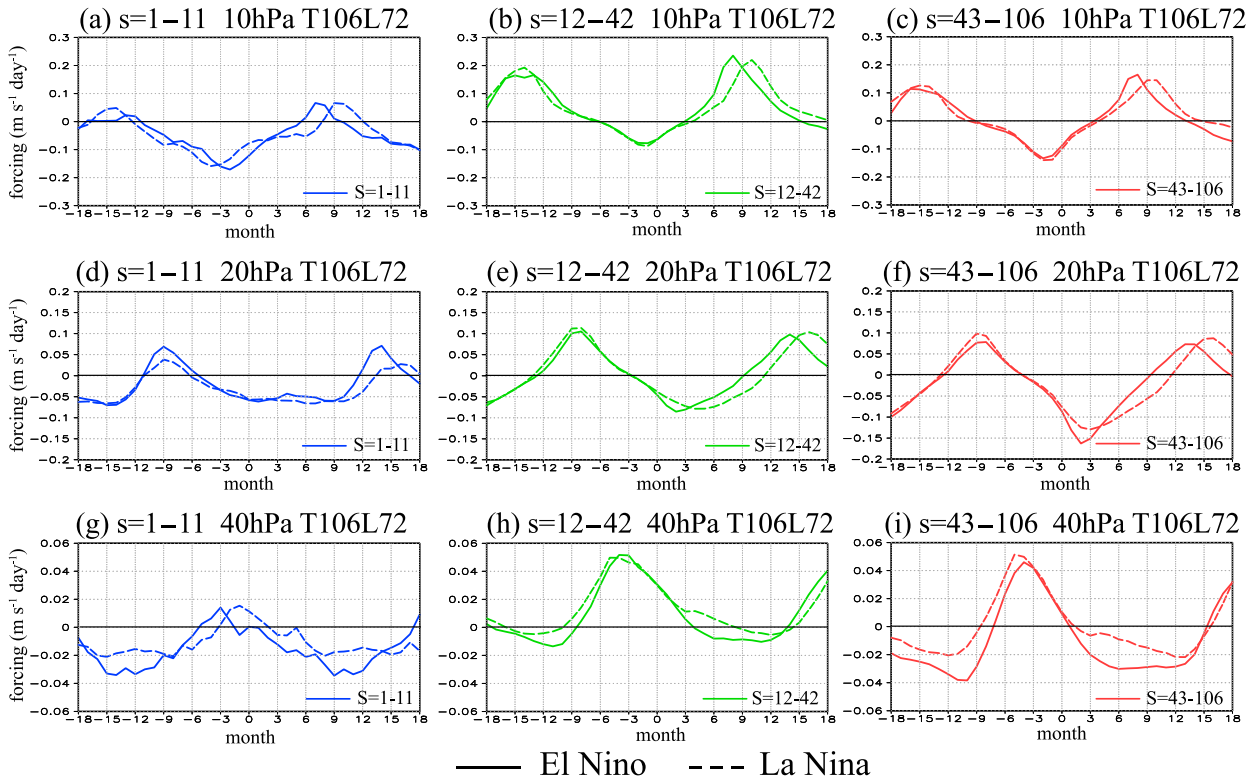


FIG. 12. As in Fig. 11, but for EP-flux divergence due to $1 \leq s \leq 11$ (blue), $12 \leq s \leq 42$ (green), and $43 \leq s \leq 106$ (red) at (a)–(c) 10, (d)–(f) 20, and (g)–(i) 40 hPa.

excitation. Figure 14a shows the zonal wavenumber–frequency spectra of outgoing longwave radiation (OLR) at 10°S – 10°N for our 100-yr El Niño simulation. Figures 14c and 14e show the El Niño over La Niña ratios of simulated OLR and precipitation for each spectral component. As shown earlier in Fig. 6, the overall equatorial precipitation is larger by about 15% for the El Niño simulation, but Fig. 14e shows that the precipitation difference has significant variation among space and time scales. The spectral components of both OLR and precipitation with $|C_x| \leq 10 \text{ m s}^{-1}$ are obviously larger in El Niño than in La Niña, similar to the result seen in Fig. 13b for $F^{(z)}$ at 123–114 hPa (i.e., just above the convective heating region). On the other hand, spectral components of OLR and precipitation for $C_x < -10 \text{ m s}^{-1}$ are smaller in the El Niño simulation than in the La Niña simulation. Most spectral components with $C_x > 10 \text{ m s}^{-1}$ are slightly smaller for precipitation but somewhat larger for OLR in El Niño than in La Niña. Note that eastward components with $1 \leq s \leq \sim 20$ and frequencies between 0 and ~ 1 cycle per day are larger for both OLR and precipitation in El Niño than for La Niña, irrespective of C_x .

While there are not sufficient real world data to compute the detailed space–time spectra of the wave

fluxes, available satellite datasets can provide some comparison for the space–time spectra of variables relating to the convective source for the waves. In our study we have used brightness temperature (T_b) data from the cloud archive user service (CLAUS, Robinson 2013) for the period from July 1983 to June 2009 (~ 26 years) and the TRMM 3B42, version 7 (Huffman et al. 2014) precipitation data from January 1998 to July 2017 (~ 19.5 years). The data are available globally on a 3-hourly $0.5^{\circ} \times 0.5^{\circ}$ longitude–latitude grid for CLAUS and on a 3-hourly $0.25^{\circ} \times 0.25^{\circ}$ grid for TRMM 3B42. The combined Fourier–wavelet transform, defined as a combination of the Fourier transform in longitude and the wavelet transform in time, was used to calculate spectra for these observed quantities (Kikuchi 2014). This method provides an instantaneous space–time spectrum at any given time. First, the spectra were monthly averaged, and then the composited El Niño and La Niña spectra were obtained by the same procedure introduced in section 2. However, the records of both CLAUS and TRMM satellite data are considerably shorter than for the SST data we used to define the ENSO composites (e.g., for January we had El Niño, 15 samples for SST, as shown in Table 1; but there are only 5 samples for

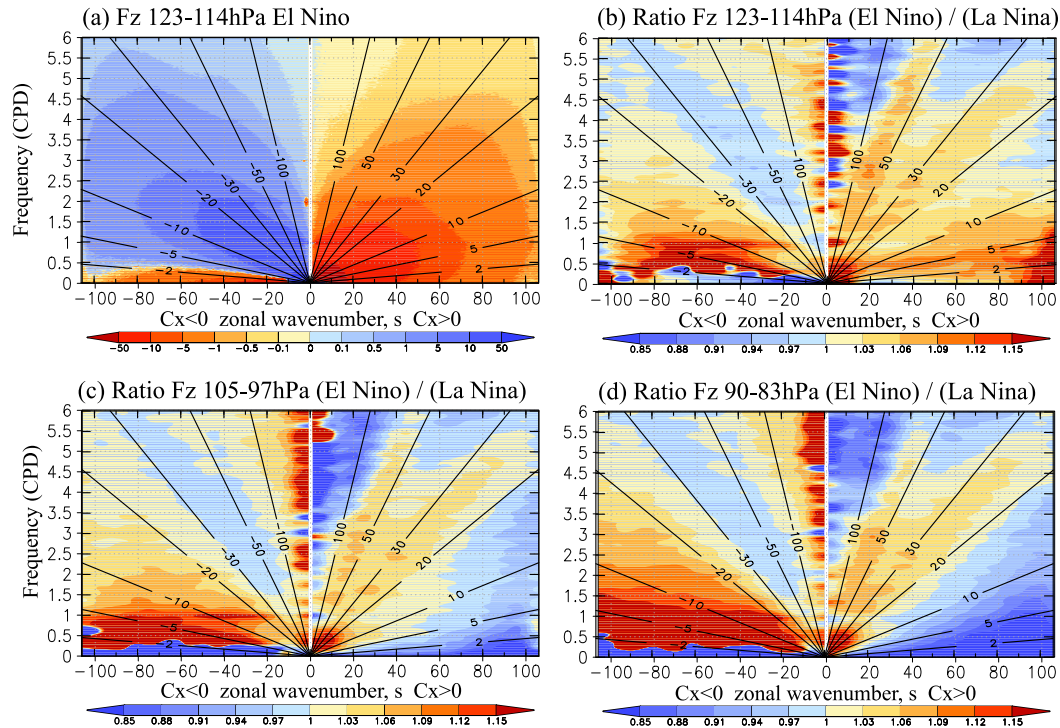


FIG. 13. (a) Zonal wavenumber–frequency spectra of the vertical component of the EP flux in the El Niño MIROC-AGCM run averaged over 123–114 hPa and 10°S – 10°N . Ratio of El Niño to La Niña for the vertical component of EP flux averaged over (b) 123–114, (c) 105–97, and (d) 90–83 hPa and 10°S – 10°N . The shaded intervals are $\pm 0.1, 0.5, 1, 5, 10,$ and $50 \text{ kg s}^{-2} \text{ wavenumber}^{-1} \text{ cpd}^{-1}$ in (a). Shaded intervals are 0.03 in (b)–(d).

CLAUS and TRMM; while, of course, our simulations provide 100 samples for the model).

Figure 14b is the same as Fig. 14a but for observed CLAUS T_b spectra in El Niño. The overall characteristics are similar to the MIROC-AGCM simulated OLR. Figures 14d and 14f show the El Niño to La Niña spectral ratio for CLAUS T_b and TRMM precipitation. In the CLAUS data, larger T_b power in El Niño is found in the domain with $|C_x| \leq 10 \text{ m s}^{-1}$, which is similar to the model results. Smaller spectral power with $C_x < -10 \text{ m s}^{-1}$ in El Niño is also found in the T_b spectra (also seen in the model), although the minimum ratio is found along $\sim -30 \text{ m s}^{-1}$ in the CLAUS observations in contrast to $\sim -15 \text{ m s}^{-1}$ in the model. In the T_b observations (Fig. 14b) there is an enhancement of the power at high frequencies (greater than $\sim 2.5 \text{ cpd}$) and very high phase speeds ($|C_x| > \sim 100 \text{ m s}^{-1}$) that appears also in the El Niño-to-La Niña ratio (Fig. 14d); this has no counterpart in the OLR spectra from our model simulation (Fig. 14c).

In the TRMM data, much larger spectral power is seen in El Niño for $\sim 60 \leq s \leq 60$ and frequencies less than 1 cpd. Interestingly, westward components with $-10 \leq C_x \leq 0 \text{ m s}^{-1}$ are much larger, including for large zonal wavenumbers, as seen in the model

precipitation, OLR, and observed CLAUS T_b data. Eastward components with $1 \leq s \leq \sim 20$ and $0 < \text{cycles per day} < \sim 1$ are larger in El Niño for both the CLAUS T_b and TRMM precipitation, as also seen in the model results. Comparing these two limited record observational datasets with the model, more active convection with $|C_x| \leq \sim 10 \text{ m s}^{-1}$ in El Niño than La Niña is likely, although more detailed analyses and longer observed data lengths may be required to prove this hypothesis.

Herein, we propose the possible mechanisms of ENSO modulation of the QBO by analyzing the MIROC-AGCM and comparing with reanalysis and observational data. Figure 15 is a schematic summarizing our diagnosis of the ENSO modulation of the tropical atmospheric circulation in MIROC-AGCM. Key points that emerged from our analysis are:

- (i) The period of the QBO is shorter in El Niño, and the difference in the QBO mean zonal wind tendency is obvious, especially in the lower stratosphere.
- (ii) The Walker circulation is weaker in El Niño, and so less wave filtering in the upper troposphere may occur, partially contributing to more wave propagation into the stratosphere.

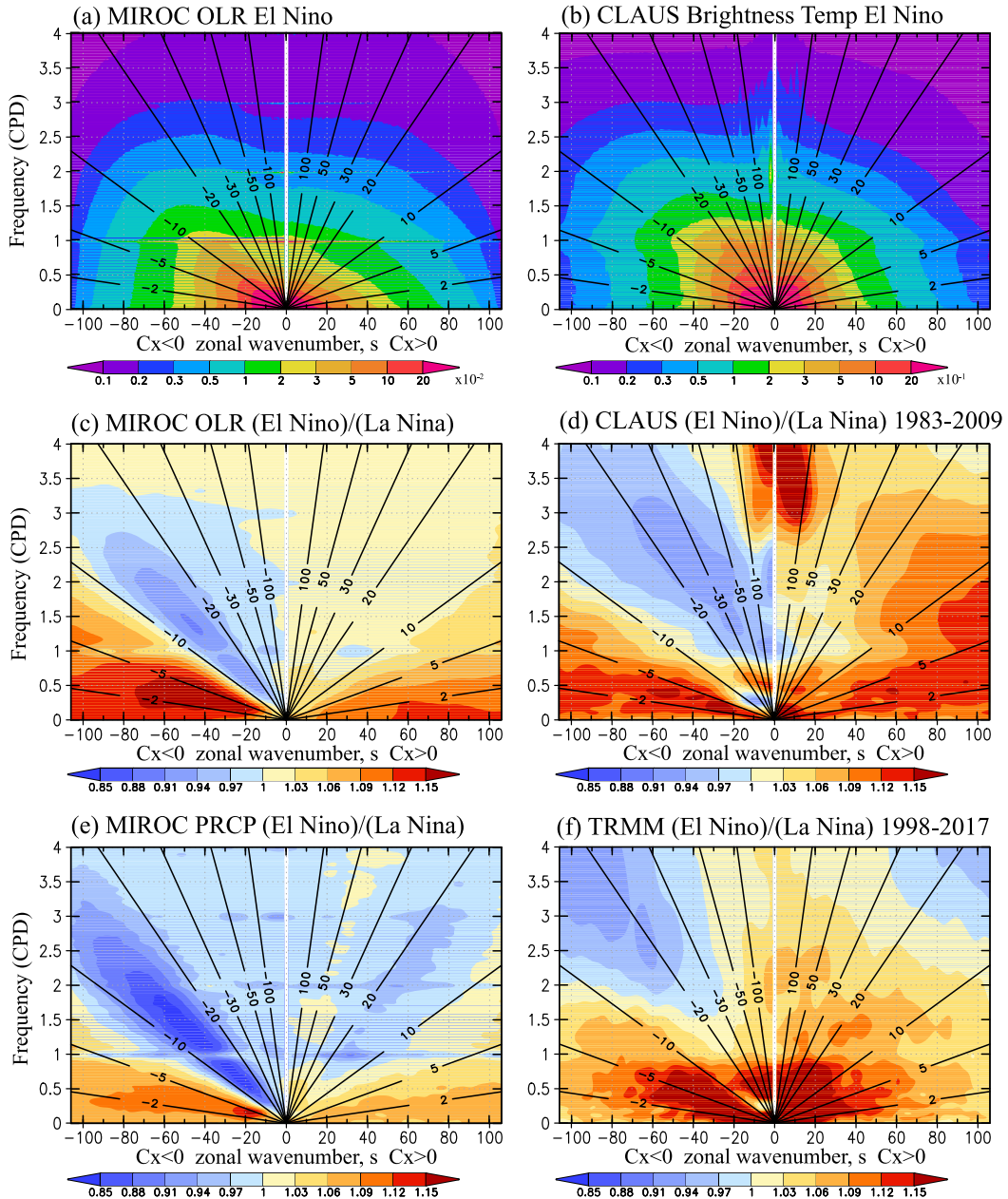


FIG. 14. (a) Zonal wavenumber–frequency spectra of OLR in the MIROC-AGCM El Niño run for a 100-yr average at 10°S–10°N and (b) those of brightness temperature data from the cloud archive user service (CLAUS) during El Niño months from July 1983 to June 2009 at 10°S–10°N. Ratio of El Niño to La Niña for (c) simulated OLR, (d) CLAUS brightness temperature, (e) simulated precipitation, and (f) TRMM 3B42. TRMM data employed are for January 1998–July 2017. Shaded intervals are 0.1, 0.2, 0.3, 0.5, 1, 2, 3, 5, 10, and $20 \times 10^{-2} \text{ W}^2 \text{ m}^{-4} \text{ wavenumber}^{-1} \text{ cpd}^{-1}$ in (a) and $0.1, 0.2, 0.3, 0.5, 1, 2, 3, 5, 10, \text{ and } 20 \times 10^{-1} \text{ K}^2 \text{ wavenumber}^{-1} \text{ cpd}^{-1}$ in (b). The shaded intervals are 0.03 in (c)–(f).

- (iii) Equatorial mean precipitation is $\sim 15\%$ larger in El Niño than in La Niña, consistent with larger wave momentum fluxes seen in the uppermost troposphere.
- (iv) Quite distinct differences in the wave forcing are found in small-scale gravity waves with zonal

- wavenumbers ≥ 43 (zonal wavelengths $< \sim 930 \text{ km}$) in the lower stratosphere.
- (v) The space–time spectrum of low-latitude convection with $|C_x| < 10 \text{ m s}^{-1}$, shows considerable enhancement in El Niño versus La Niña. This should lead to an enhancement of the wave forcing for these

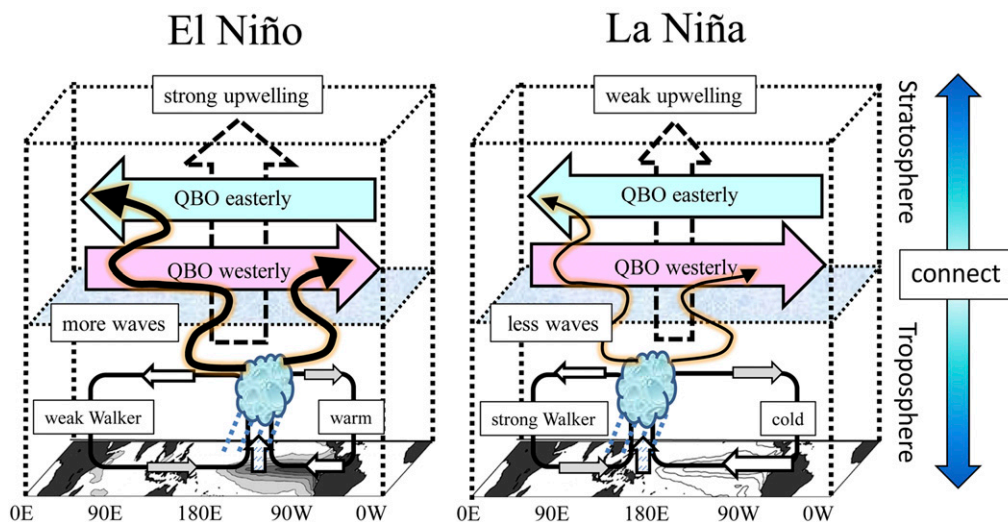


FIG. 15. Schematic illustration of the Walker circulation (thick vector), gravity waves (black vector), QBO zonal wind (blue and pink), and equatorial residual vertical velocity (dashed vector) for (left) El Niño and (right) La Niña.

relatively slow waves which may be expected to contribute most importantly to the mean-flow accelerations in the lowermost reaches of the QBO. It is noteworthy that this aspect of the ENSO modulation of convection is found also in satellite measurements of precipitation and cloud brightness temperatures.

- (vi) The tropical upwelling associated with the BDC is enhanced in El Niño, consistent with wave propagation changes due to westerly wind anomalies in midlatitudes. However, the expected effects of the enhanced BDC during El Niño in delaying downward QBO phase progression are overcome by enhanced wave driving, resulting in a shorter QBO period in El Niño than in La Niña.

5. ENSO modulation of the QBO in the MIROC-ESM with fixed parameterized gravity wave sources

In this section, results from the MIROC-ESM are discussed. As introduced in section 2, the horizontal resolution of the MIROC-ESM is T42, and, thus, small-scale gravity waves with $s \geq 43$ cannot be explicitly represented. The MIROC-ESM used the Hines-type nonorographic GWP with a prescribed wave source at the assumed “launch level” of 650 hPa that is constant in time and throughout the tropics (Watanabe et al. 2011). Therefore, the upward flux at 650 hPa of the parameterized GWs, and its assumed space–time spectrum, does not respond to the El Niño versus La Niña differences in convection.

Figure 16 shows time series of the QBO periods in the 100-yr El Niño and La Niña integrations. In contrast to the MIROC-AGCM results (Fig. 3), mean QBO periods are nearly identical between the El Niño (23.7 months) and La Niña (24.1 months) cases, and this difference is not statistically significant. We have confirmed that the El Niño versus La Niña differences for the Walker circulation, precipitation, as well as the latitude–height sections of zonal-mean temperature, zonal wind, EP-flux divergence, orographic GWP forcing, and equatorial tropical upwelling are similar to those in the MIROC-AGCM (not shown, see Figs. 5–9 for the MIROC-AGCM results).

We constructed composite QBOs for the 10°S–10°N-averaged fields from the MIROC-ESM integrations following the same procedure used for MIROC-AGCM in the previous section. Figure 17 shows the resulting composited mean zonal wind together with measures of wave driving of the mean-flow accelerations. In Figs. 17a and 17b we show the sum of the resolved wave forcing (EP-flux divergence) plus parameterized nonorographic GW driving [corresponding to \bar{X} in Eq. (5)]. Figures 17c–f display the resolved and parameterized wave driving separately. The general pattern of total wave driving of the mean-flow accelerations seen in Figs. 17a and 17b is similar to that seen for MIROC-AGCM (Fig. 10a,b). However, the total resolved wave forcing in the MIROC-ESM (Figs. 17c,d) is much smaller than that in the MIROC-AGCM. In the MIROC-ESM parameterized nonorographic gravity waves (Figs. 17e,f) contribute more to westward forcing below 30 hPa compared with the resolved waves, while the resolved

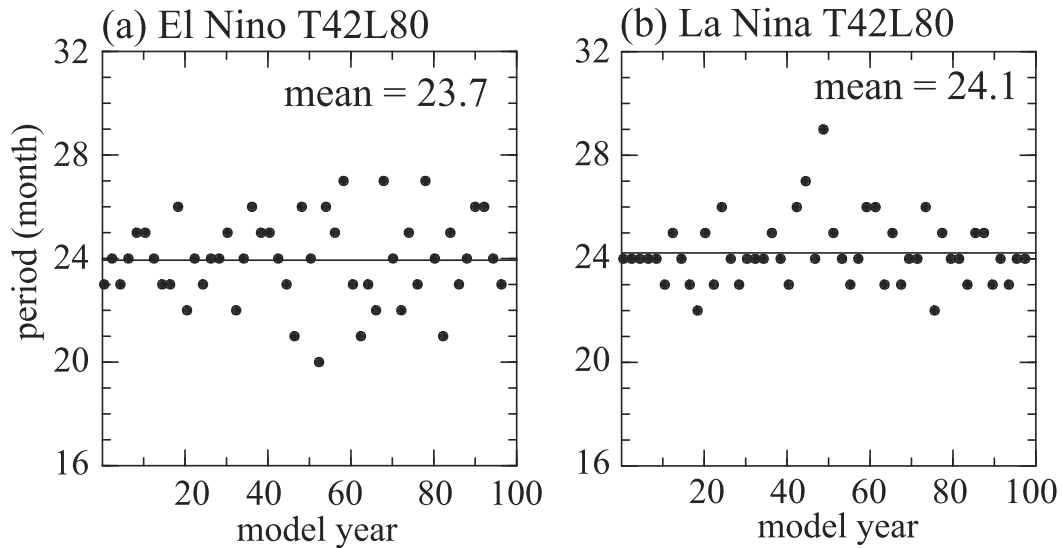


FIG. 16. As in Fig. 3, but for T42L80 MIROC-ESM. Differences in the QBO period between El Niño and La Niña are statistically insignificant.

waves contribute more to eastward forcing below 30 hPa. These results are consistent with Kawatani et al. (2010a), who used a much higher resolution, T213L256 AGCM and showed that small-scale gravity waves ($s \geq 43$) contribute to the easterly acceleration phase of the QBO, especially in the lower stratosphere, while the contribution of large-scale ($1 \leq s \leq 11$) waves is relatively large in the westerly acceleration phase.

Figure 18 shows the terms in the zonal-mean equatorial zonal momentum budget through the QBO composite cycle for MIROC-ESM in the same format as Fig. 11, but including forcing due to parameterized nonorographic GWs. The zonal wind tendency is very similar between El Niño and La Niña, consistent with the nearly identical mean QBO periods in the two cases. At 40 hPa, the resolved westward wave forcing (EP-flux divergence) in El Niño is slightly larger than in La Niña (see months 1–7), but the differences are small compared with those in the MIROC-AGCM (Fig. 11f). This is understandable because large El Niño versus La Niña differences in the EP-flux divergence in the MIROC-AGCM are primarily due to resolved waves with $s \geq 43$ (Fig. 12i), which cannot be represented by the T42 MIROC-ESM. Interestingly, wave forcing due to parameterized subgrid nonorographic gravity waves is nearly identical between El Niño and La Niña runs at all three levels shown (10, 20, and 40 hPa).

While the QBO does not speed up in the low-resolution model, neither does it slow down, despite the enhanced upwelling. Relatively small differences in resolved waves with $s \leq 42$ and fixed sources of parameterized waves only compensate for increased tropical upwelling (not shown)

and could not overcome it, which result in the very similar QBO period seen in the El Niño and La Niña runs. The MIROC-ESM experiments are consistent with our conclusion from our MIROC-AGCM runs that GWs of relatively small scale (but still resolvable at T106) contribute critically to the ENSO modulation of the QBO. In a moderate resolution model, such as T42, a realistic ENSO modulation of the QBO presumably requires a more sophisticated parameterization of subgrid-scale GW effects.

6. Summary and conclusions

The QBO dominates the interannual variability in the tropical stratosphere and has many connections with circulation in the extratropics and the troposphere. Adequate representation of the QBO thus plays a potentially important role in both extended-range weather forecasting as well as projections of climate response to external forcing. Since the development of the first global comprehensive atmospheric simulation models, the QBO has been a particular challenge to simulate and such simulations depend on the subgrid parameterization of moist convection and typically also on parameterizations of the mean-flow effects of GWs generated in the troposphere. Given this dependence on rather poorly constrained parameterizations, it is interesting to examine how the model QBO simulations respond to external forcing of the atmosphere. The relatively recent observational findings of Taguchi (2010) and Yuan et al. (2014) that there are systematic differences in the average behavior of the QBO between El Niño and

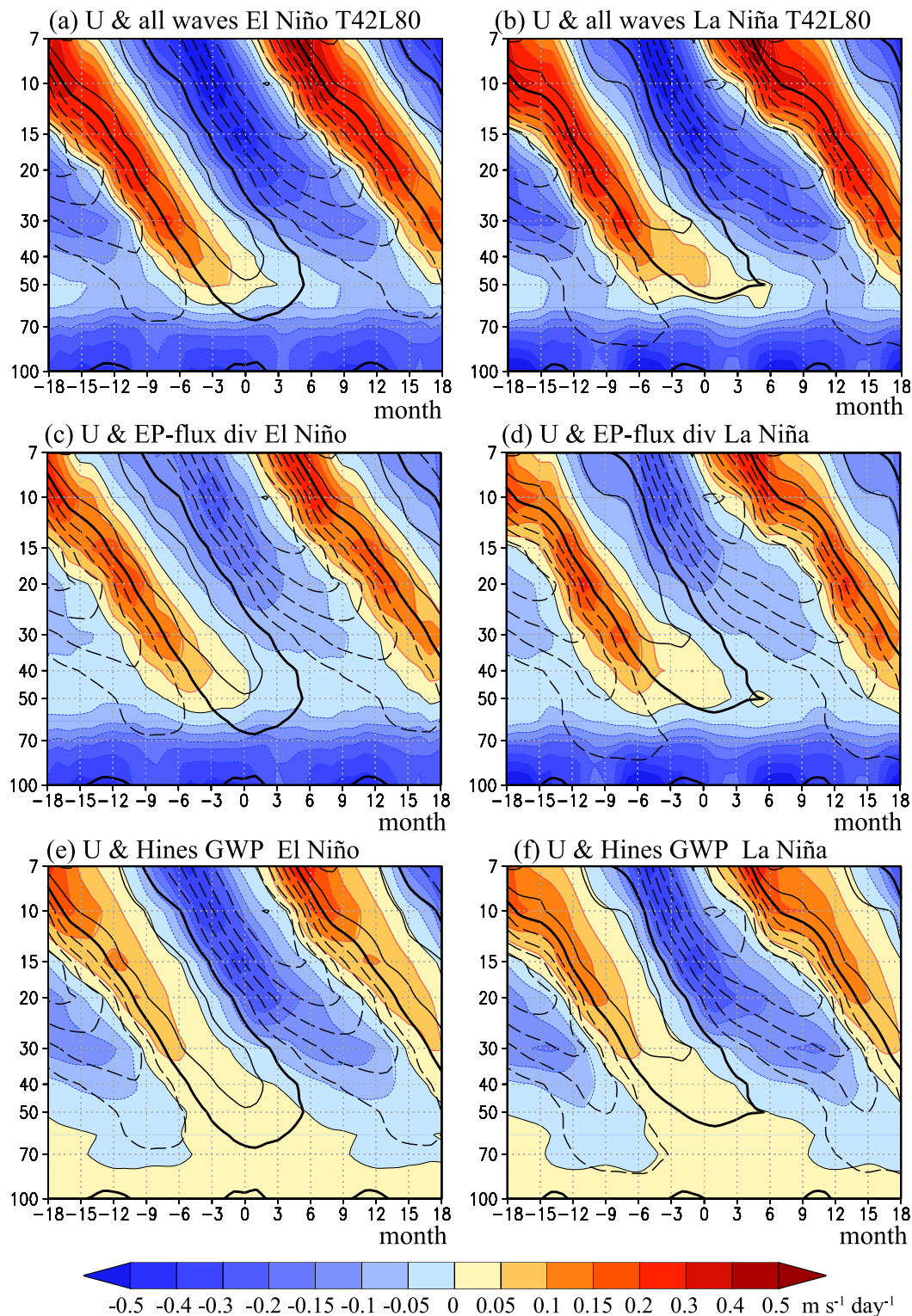


FIG. 17. As in Fig. 10, but for (left) El Niño and (right) La Niña, for (a),(b) resolved plus Hines-type parameterized nonorographic wave forcing, (c),(d) resolved waves, and (e),(f) parameterized waves for the T42L80 MIROC-ESM.

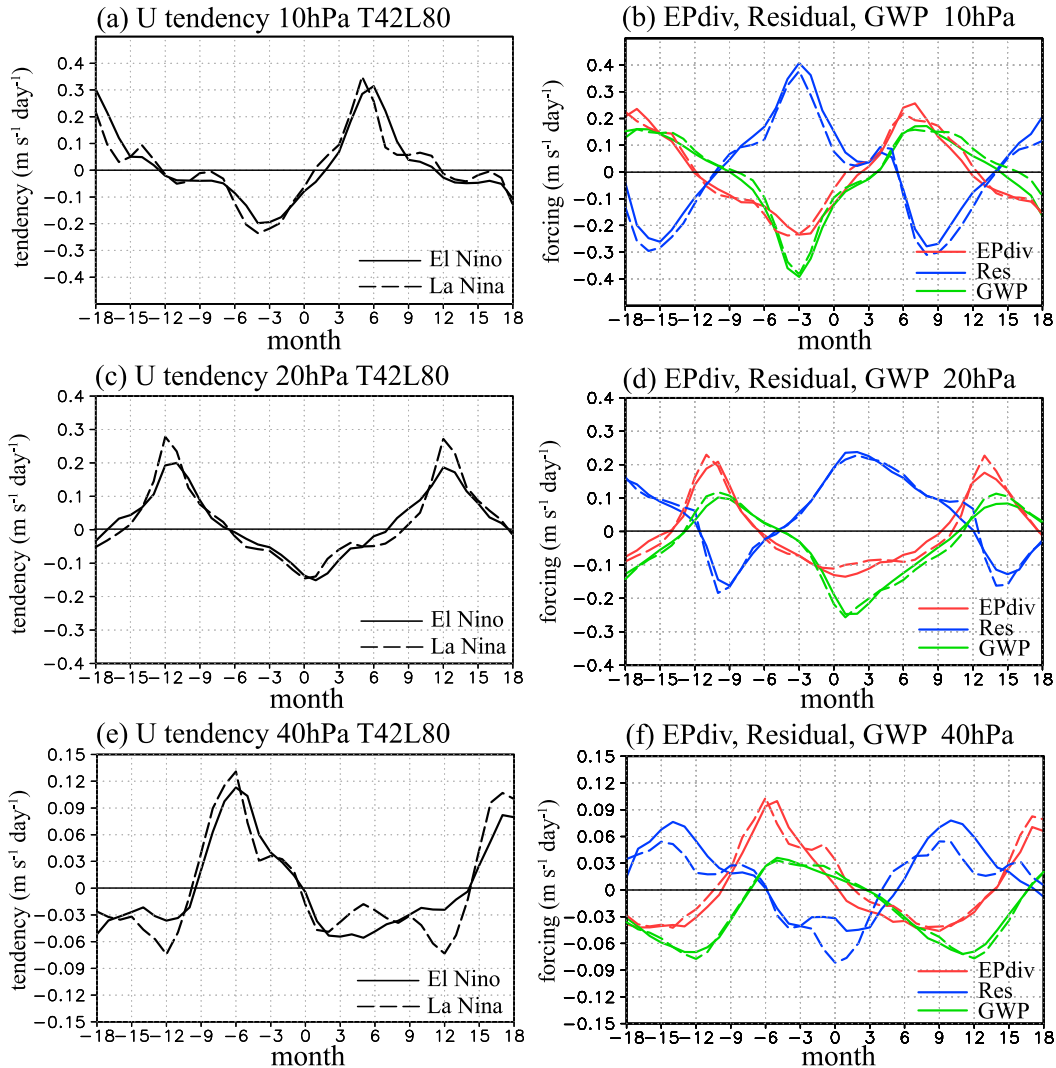


FIG. 18. As in Fig. 11, but for MIROC-ESM simulations. Note that the green lines in (b), (d), and (f) show the parameterized nonorographic gravity wave forcing.

La Niña periods provided the motivation of our investigation of this phenomenon in model simulations.

In our study we adopted a simple procedure to specify boundary conditions appropriate for moderately strong El Niño and La Niña conditions and then performed long integrations for each of these cases. The integrations were conducted first with the high-resolution MIROC-AGCM and then repeated with the moderate-resolution MIROC-ESM. The MIROC-AGCM is notable for spontaneously simulating a fairly realistic stratospheric QBO, despite having no parameterization of the effects of subgrid-scale nonorographic GWs, while the MIROC-ESM is more typical of most current global models in that it requires a GW parameterization to produce a QBO in the tropical stratosphere. Our analysis of the MIROC-AGCM simulation showed that

there was a significantly shorter QBO mean period for the El Niño case than for La Niña, in qualitative agreement with observations.

We showed that the El Niño versus La Niña QBO period differences in the simulations could be interpreted within a fairly simple conceptual framework. Specifically, we expect the simulation to be affected by two competing effects, namely the role of mean upwelling in delaying the QBO phase descent and the role of upward-propagating waves in driving the accelerations of the mean flow through the QBO cycle. In both of our models the El Niño state was found to have a more intense mean upwelling in the tropical lower stratosphere [in agreement with earlier expectations, see Domeisen et al. (2019)]. This means that the wave forcing of the QBO mean-flow accelerations must also increase in El Niño in

order to compensate, and indeed our diagnosis of the wave fluxes showed this. However, there were important differences in the responses of the MIROC-AGCM and MIROC-ESM in this regard. Notably the contribution of waves with $s \geq 43$ to the ENSO modulation of QBO mean-flow accelerations is quite important in the MIROC-AGCM simulations, while these waves are not explicitly represented in the MIROC-ESM simulations. Given that assumed tropospheric sources for the parameterized small-scale waves was fixed in MIROC-ESM, it is not surprising that this model did not predict the substantial El Niño versus La Niña mean period difference seen in the MIROC-AGCM (and in observations).

We analyzed the space–time spectrum of the wave fluxes near the equator in the MIROC-AGCM simulations and also computed the spectra of measures of tropical convection (which should account for much of the excitation of upward-propagating waves). We showed the computed El Niño versus La Niña ratios as a function of wavenumber and frequency for both the wave fluxes and the measures of convection. The increased wave fluxes entering the equatorial stratosphere in El Niño are attributable to the increased convective wave forcing seen at most wavenumbers and frequencies. Less wave filtering by the weakened Walker circulation in El Niño may also partially contribute to larger wave fluxes in the lowermost stratosphere during El Niño. A novel feature of our study was the comparison of the El Niño versus La Niña space–time spectra of simulated convection with satellite observations of cloud brightness temperature and total precipitation.

Differences of mean QBO periods between El Niño and La Niña in the MIROC-AGCM (~ 2.2 months) are smaller than those estimated by Taguchi (2010). Of course, our experiment with annually repeating prescribed SST does not actually duplicate the conditions experienced by the real atmosphere, making the comparison with Taguchi's observed composites somewhat imprecise. However, the apparently somewhat weak sensitivity of the QBO period to ENSO in the MIROC-AGCM may reflect inadequacies in some aspects of the model performance. A notable limitation is the T106 horizontal resolution. Kawatani et al. (2010a) found by using T213 AGCM that GWs with $s \geq 107$ largely contribute to the QBO driving, especially in the easterly shear phase. The present T106 MIROC-AGCM could not represent such smaller-scale GWs, and El Niño minus La Niña wave flux differences thus may be underestimated, resulting in smaller QBO period differences. The weaker amplitude of the QBO in the lower stratosphere, which is common in many other AGCMs, also may result in some discrepancy compared with the real atmosphere.

In this paper, we focused on zonal-mean forcing of the stratospheric circulation. As Geller et al. (2016a,b) noted, the period of the modeled QBO depends mainly on the magnitude of the zonally averaged gravity wave momentum fluxes entering the equatorial stratosphere and less on the longitudinal distribution of fluxes. Kawatani et al. (2009, 2010b) have shown that the longitudinal variations of equatorial trapped waves, and three-dimensional propagating inertia–gravity waves depend significantly on the tropospheric background winds and wave sources. It would be interesting to analyze the ENSO modulation of the three-dimensional wave forcing as well as tropical upwelling, which must show large differences between El Niño and La Niña. This may be investigated in a future study.

In the observed record there are cycle-to-cycle variations of QBO period that are clearly not explained purely by ENSO modulation. Even in our model integrations which had imposed repeated annual cycles of SST and no other interannual external forcing, there are significant cycle-to-cycle QBO variations apparent (so, for example, in our MIROC-AGCM El Niño run, the individual QBO cycles we identified had periods ranging from 17 to 26 months; see Fig. 3). Despite this considerable internally excited variability, it is noteworthy that in our 200 years of integration (for each of two models) we always saw a reasonably standard progression of wind evolution through each QBO cycle. We never saw anything approaching the extreme QBO disruption seen in the real atmosphere in early 2016 (Osprey et al. 2016; Newman et al. 2016). There has been speculation that the strong (and somewhat unusual) El Niño in 2015 may have contributed to the unusual QBO development (Barton and McCormack 2017). Further model integrations with a variety of SST forcing may be useful in investigating a fuller (and possibly more realistic) range of QBO behavior.

Ours is one of the first global model studies of the ENSO–QBO interaction, but there has been more experience in model studies of another forced problem, namely the response of the QBO in global warming simulations (see Kawatani et al. 2011; Kawatani and Hamilton 2013; Richter et al. 2019, manuscript submitted to *Quart. J. Roy. Meteor. Soc.*, and references therein). El Niño conditions might be expected to provide an analog of a globally warmed climate state, since in the zonal mean El Niño is characterized by a warmer equatorial troposphere and enhanced precipitation. The present MIROC-AGCM simulations are of interest in this regard as they have been performed with exactly the same model as used by Kawatani et al. (2011) in global warming (forced by doubled atmospheric carbon dioxide concentrations) and present-day integrations.

In the global warming case Kawatani et al. diagnosed increased mean upwelling in the tropical lower stratosphere as well as enhanced resolved wave fluxes. However, the details are somewhat different and the overall effect of the warmed climate is actually a period increase, showing that El Niño is a somewhat inadequate analog for the expected effects of global warming. However, it is valuable to test models employed for climate projections by using the ENSO cycle (for which we can find actual observations of such features as the QBO period and the spectrum of tropical convection).

The Stratosphere–Troposphere Processes And their Role in Climate (SPARC) Quasi-Biennial Oscillation initiative (QBOi) has begun extensive global model inter-comparisons with a focus on the stratospheric QBO simulation (Butchart et al. 2018). Four of the 11 AGCMs now involved in QBOi use GWPs with variable wave sources, six have fixed sources for the GWPs and one (MIROC-AGCM) has no nonorographic GWP. Richter et al. (2019, manuscript submitted to *Quart. J. Roy. Meteor. Soc.*) show that the changes in period of the QBO in warming climate simulations varied quite significantly among these models. Some models projected longer mean periods and some shorter mean periods for the QBO in a future warmer climate. The QBOi now has a project underway to analyze multimodel ENSO–QBO experiments similar to those described here with an eye to providing further insight into the response of QBO in state-of-the-art AGCMs to external forcing.

Acknowledgments. We express our gratitude to two anonymous reviewers for their valuable comments on the original manuscript. YK was supported by Japan Society for Promotion of Science (JSPS) KAKENHI Grants JP15KK0178, JP17K18816, JP18H01286, and by the Environment Research and Technology Development Fund (2-1904) of the Environmental Restoration and Conservation Agency of Japan. YK, KH, and KK were supported by the Japan Agency for Marine–Earth Science and Technology (JAMSTEC) through its sponsorship of research at the International Pacific Research Center. This is IPRC Publication Number 1403. KK also acknowledges support from NOAA grant NA17OAR4310250. This study was partly supported by the Japan Science and Technology Agency (JST) as part of the Belmont Forum and JST CREST Grant JPMJCR1663. We used the CLAU archive held at the British Atmospheric Data Centre, produced using ISCCP source data distributed by the NASA Langley Data Center. The TRMM 3B42 data were provided by the NASA, which develop and compute the TRMM 3B42 as a contribution to TRMM, and archived at the NASA GES DISC. The numerical simulations in this study were performed using the

JAMSTEC Earth Simulator. The GFD-DENNOU Library and GrADS were used to draw the figures.

REFERENCES

- Alexander, M. J., and Coauthors, 2010: Recent developments in gravity-wave effects in climate models and the global distribution of gravity-wave momentum flux from observations and models. *Quart. J. Roy. Meteor. Soc.*, **136**, 1103–1124, <https://doi.org/10.1002/qj.637>.
- Andrews, D. G., J. R. Holton, and C. B. Leovy, 1987: *Middle Atmosphere Dynamics*. Academic Press, 489 pp.
- Baldwin, M. P., and Coauthors, 2001: The quasi-biennial oscillation. *Rev. Geophys.*, **39**, 179–229, <https://doi.org/10.1029/1999RG000073>.
- Barton, C. A., and J. P. McCormack, 2017: Origin of the 2016 QBO disruption and its relationship to extreme El Niño events. *Geophys. Res. Lett.*, **44**, 11 150–11 157, <https://doi.org/10.1002/2017GL075576>.
- Beres, J. H., M. J. Alexander, and J. R. Holton, 2004: A method of specifying the gravity wave spectrum above convection based on latent heating properties and background wind. *J. Atmos. Sci.*, **61**, 324–337, [https://doi.org/10.1175/1520-0469\(2004\)061<0324:AMOSTG>2.0.CO;2](https://doi.org/10.1175/1520-0469(2004)061<0324:AMOSTG>2.0.CO;2).
- Boer, G. J., and K. Hamilton, 2008: QBO influence on extratropical predictive skill. *Climate Dyn.*, **31**, 987–1000, <https://doi.org/10.1007/s00382-008-0379-5>.
- Butchart, N., and Coauthors, 2018: Overview of experiment design and comparison of models participating in phase 1 of the SPARC Quasi-Biennial Oscillation initiative (QBOi). *Geosci. Model Dev.*, **11**, 1009–1032, <https://doi.org/10.5194/gmd-11-1009-2018>.
- Calvo, N., R. R. Garcia, W. J. Randel, and D. R. Marsh, 2010: Dynamical mechanism for the increase in tropical upwelling in the lowermost tropical stratosphere during warm ENSO events. *J. Atmos. Sci.*, **67**, 2331–2340, <https://doi.org/10.1175/2010JAS3433.1>.
- Collimore, C. C., D. W. Martin, M. H. Hitchman, A. Huesmann, and D. E. Waliser, 2003: On the relationship between the QBO and tropical deep convection. *J. Climate*, **16**, 2552–2568, [https://doi.org/10.1175/1520-0442\(2003\)016<2552:OTRBTQ>2.0.CO;2](https://doi.org/10.1175/1520-0442(2003)016<2552:OTRBTQ>2.0.CO;2).
- Domeisen, D. I. V., C. I. Garfinkel, and A. H. Butler, 2019: The teleconnection of El Niño–Southern Oscillation to the stratosphere. *Rev. Geophys.*, **57**, 5–47, <https://doi.org/10.1029/2018RG000596>.
- Dunkerton, T. J., 1997: The role of gravity waves in the quasi-biennial oscillation. *J. Geophys. Res.*, **102**, 26 053–26 076, <https://doi.org/10.1029/96JD02999>.
- , 2017: Nearly identical cycles of the quasi-biennial oscillation in the equatorial lower stratosphere. *J. Geophys. Res. Atmos.*, **122**, 8647–8493, <https://doi.org/10.1002/2017JD026542>.
- , and D. P. Delisi, 1985: Climatology of the equatorial lower stratosphere. *J. Atmos. Sci.*, **42**, 376–3961, [https://doi.org/10.1175/1520-0469\(1985\)042<0376:COTELS>2.0.CO;2](https://doi.org/10.1175/1520-0469(1985)042<0376:COTELS>2.0.CO;2).
- , and M. P. Baldwin, 1991: Quasi-biennial modulation of planetary-wave fluxes in the Northern Hemisphere winter. *J. Atmos. Sci.*, **48**, 1043–1061, [https://doi.org/10.1175/1520-0469\(1991\)048<1043:QBMOPW>2.0.CO;2](https://doi.org/10.1175/1520-0469(1991)048<1043:QBMOPW>2.0.CO;2).
- Ern, M., P. Preusse, M. Krebsbach, M. G. Mlynarczyk, and J. M. Russell III, 2008: Equatorial wave analysis from SABER and ECMWF temperatures. *Atmos. Chem. Phys.*, **8**, 845–869, <https://doi.org/10.5194/acp-8-845-2008>.

- Evan, S., M. J. Alexander, and J. Duhia, 2012: Model study of intermediate-scale tropical inertia–gravity waves and comparison to TWP-ICE campaign observations. *J. Atmos. Sci.*, **69**, 591–610, <https://doi.org/10.1175/JAS-D-11-051.1>.
- Geller, M. A., W. Shen, M. H. Zhang, and W. W. Tan, 1997: Calculation of the stratospheric QBO for time-varying forcing. *J. Atmos. Sci.*, **54**, 883–894, [https://doi.org/10.1175/1520-0469\(1997\)054<0883:COTSQB>2.0.CO;2](https://doi.org/10.1175/1520-0469(1997)054<0883:COTSQB>2.0.CO;2).
- , T. H. Zhou, and W. Yuan, 2016a: The QBO, gravity waves forced by tropical convection, and ENSO. *J. Geophys. Res. Atmos.*, **121**, 8886–8895, <https://doi.org/10.1002/2015JD024125>.
- , and Coauthors, 2016b: Modeling the QBO—Improvements resulting from higher model vertical resolution. *J. Adv. Model. Earth Syst.*, **8**, 1092–1105, <https://doi.org/10.1002/2016MS000699>.
- Gray, L. J., J. A. Anstey, Y. Kawatani, H. Lu, S. M. Osprey, and V. Schenzinger, 2018: Surface impacts of the Quasi Biennial Oscillation. *Atmos. Chem. Phys.*, **18**, 8227–8247, <https://doi.org/10.5194/acp-18-8227-2018>.
- Hamilton, K., R. J. Wilson, and R. Hemler, 1999: Middle atmosphere simulated with high vertical and horizontal resolution versions of a GCM: Improvements in the cold pole bias and generation of a QBO-like oscillation in the tropics. *J. Atmos. Sci.*, **56**, 3829–3846, [https://doi.org/10.1175/1520-0469\(1999\)056<3829:MASHWHV>2.0.CO;2](https://doi.org/10.1175/1520-0469(1999)056<3829:MASHWHV>2.0.CO;2).
- Hasumi, H., and S. Emori, 2004: K-1 coupled GCM (MIROC) description. K-1 Tech. Rep. 1, University of Tokyo, 34 pp., http://ccsr.aori.u-tokyo.ac.jp/~hasumi/miroc_description.pdf.
- Hines, C. O., 1997: Doppler-spread parameterization of gravity wave momentum deposition in the middle atmosphere, Part 2: Broad and quasi monochromatic spectra, and implementation. *J. Atmos. Sol.-Terr. Phys.*, **59**, 387–400, [https://doi.org/10.1016/S1364-6826\(96\)00080-6](https://doi.org/10.1016/S1364-6826(96)00080-6).
- Holton, J. R., and R. S. Lindzen, 1972: An updated theory for the quasi-biennial cycle of the tropical stratosphere. *J. Atmos. Sci.*, **29**, 1076–1080, [https://doi.org/10.1175/1520-0469\(1972\)029<1076:AUTFTQ>2.0.CO;2](https://doi.org/10.1175/1520-0469(1972)029<1076:AUTFTQ>2.0.CO;2).
- , and H.-C. Tan, 1980: The influence of the equatorial quasi-biennial oscillation on global circulation at 50 mb. *J. Atmos. Sci.*, **37**, 2200–2208, [https://doi.org/10.1175/1520-0469\(1980\)037<2200:TIOTEQ>2.0.CO;2](https://doi.org/10.1175/1520-0469(1980)037<2200:TIOTEQ>2.0.CO;2).
- Huffman, G., D. Bolvin, D. Braithwaite, K. Hsu, R. Joyce, and P. Xie, 2014: Integrated Multi-satellite Retrievals for GPM (IMERG), version 4.4. NASA's Precipitation Processing Center, accessed 31 March 2015, <ftp://arthurhou.pps.eosdis.nasa.gov/gpmdata/>.
- Kawatani, Y., and K. Hamilton, 2013: Weakened stratospheric quasi-biennial oscillation driven by increased tropical mean upwelling. *Nature*, **497**, 478–481, <https://doi.org/10.1038/nature12140>.
- , M. Takahashi, K. Sato, S. P. Alexander, and T. Tsuda, 2009: Global distribution of atmospheric waves in the equatorial upper troposphere and lower stratosphere: AGCM simulation of sources and propagation. *J. Geophys. Res.*, **114**, D01102, <https://doi.org/10.1029/2008JD010374>.
- , K. Sato, T. J. Dunkerton, S. Watanabe, S. Miyahara, and M. Takahashi, 2010a: The roles of equatorial trapped waves and internal inertia–gravity waves in driving the quasi-biennial oscillation. Part I: Zonal mean wave forcing. *J. Atmos. Sci.*, **67**, 963–980, <https://doi.org/10.1175/2009JAS3222.1>.
- , —, —, —, —, and —, 2010b: The roles of equatorial trapped waves and internal inertia–gravity waves in driving the quasi-biennial oscillation. Part II: Three-dimensional distribution of wave forcing. *J. Atmos. Sci.*, **67**, 981–997, <https://doi.org/10.1175/2009JAS3223.1>.
- , K. Hamilton, and S. Watanabe, 2011: The quasi-biennial oscillation in a double CO₂ climate. *J. Atmos. Sci.*, **68**, 265–283, <https://doi.org/10.1175/2010JAS3623.1>.
- , J. N. Lee, and K. Hamilton, 2014: Interannual variations of stratospheric water vapor in MLS observations and climate model simulations. *J. Atmos. Sci.*, **71**, 4072–4085, <https://doi.org/10.1175/JAS-D-14-0164.1>.
- , K. Hamilton, L. J. Gray, S. M. Osprey, S. Watanabe, and Y. Yamashita, 2019: The effects of a well-resolved stratosphere on the simulated boreal winter circulation in a climate model. *J. Atmos. Sci.*, **76**, 1203–1226, <https://doi.org/10.1175/JAS-D-18-0206.1>.
- Kidston, J., A. A. Scaife, S. C. Hardiman, D. M. Mitchell, N. Butchart, M. P. Baldwin, and L. J. Gray, 2015: Stratospheric influence on tropospheric jet streams, storm tracks and surface weather. *Nat. Geosci.*, **8**, 433–440, <https://doi.org/10.1038/ngeo2424>.
- Kikuchi, K., 2014: An introduction to combined Fourier-wavelet transform and its application to convectively coupled equatorial waves. *Climate Dyn.*, **43**, 1339–1356, <https://doi.org/10.1007/s00382-013-1949-8>.
- Liess, S., and M. A. Geller, 2012: On the relationship between QBO and distribution of tropical deep convection. *J. Geophys. Res.*, **117**, D03108, <https://doi.org/10.1029/2011JD016317>.
- Lindzen, R. S., and J. R. Holton, 1968: A theory of the quasi-biennial oscillation. *J. Atmos. Sci.*, **25**, 1095–1107, [https://doi.org/10.1175/1520-0469\(1968\)025<1095:ATOTQB>2.0.CO;2](https://doi.org/10.1175/1520-0469(1968)025<1095:ATOTQB>2.0.CO;2).
- Marshall, A. G., H. H. Hendon, S.-W. Son, and Y. Lim, 2017: Impact of the quasi-biennial oscillation on predictability of the Madden-Julian oscillation. *Climate Dyn.*, **49**, 1365–1377, <https://doi.org/10.1007/s00382-016-3392-0>.
- Maruyama, T., and Y. Tsuneoka, 1988: Anomalous short duration of the easterly wind phase of the QBO at 50 hPa in 1987 and its relationship to an El Niño event. *J. Meteor. Soc. Japan*, **66**, 629–634, https://doi.org/10.2151/jmsj1965.66.4_629.
- McFarlane, N. A., 1987: The effect of orographically excited gravity wave drag on the general circulation of the lower stratosphere and troposphere. *J. Atmos. Sci.*, **44**, 1775–1800, [https://doi.org/10.1175/1520-0469\(1987\)044<1775:TEOOEG>2.0.CO;2](https://doi.org/10.1175/1520-0469(1987)044<1775:TEOOEG>2.0.CO;2).
- Newman, P. A., L. Coy, S. Pawson, and L. R. Lait, 2016: The anomalous change in the QBO in 2015–2016. *Geophys. Res. Lett.*, **43**, 8791–8797, <https://doi.org/10.1002/2016GL070373>.
- Nishimoto, E., and S. Yoden, 2017: Influence of the stratospheric quasi-biennial oscillation on the Madden-Julian oscillation during austral summer. *J. Atmos. Sci.*, **74**, 1105–1125, <https://doi.org/10.1175/JAS-D-16-0205.1>.
- Osprey, S. M., N. Butchart, J. R. Knight, A. A. Scaife, K. Hamilton, J. A. Anstey, V. Schenzinger, and C. Zhang, 2016: An unexpected disruption of the atmospheric quasi-biennial oscillation. *Science*, **353**, 1424–1427, <https://doi.org/10.1126/science.aah4156>.
- Randel, W. J., R. R. Garcia, N. Calvo, and D. Marsh, 2009: ENSO influence on zonal mean temperature and ozone in the tropical lower stratosphere. *Geophys. Res. Lett.*, **39**, L15822, <https://doi.org/10.1029/2009GL039343>.
- Robinson, G., 2013: 3-hourly High Resolution Brightness Temperature (BT) images. NCAS British Atmospheric Data Centre, accessed on 16 November 2014, <http://catalogue.ceda.ac.uk/uuid/c2112bdd5f0ad698e70be6ab54c9a2ac>.
- Scaife, A. A., and Coauthors, 2014: Predictability of the quasi-biennial oscillation and its northern winter teleconnection on seasonal to decadal timescales. *Geophys. Res. Lett.*, **41**, 1752–1758, <https://doi.org/10.1002/2013GL059160>.

- Schirber, S., 2015: Influence of ENSO on the QBO: Results from an ensemble of idealized simulations. *J. Geophys. Res. Atmos.*, **120**, 1109–1122, <https://doi.org/10.1002/2014JD022460>.
- Simpson, I. R., T. G. Shepherd, and M. Sigmond, 2011: Dynamics of the lower stratospheric circulation response to ENSO. *J. Atmos. Sci.*, **68**, 2537–2556, <https://doi.org/10.1175/JAS-D-11-05.1>.
- Stevens, B., and Coauthors, 2013: Atmospheric component of the MPI-M Earth System Model: ECHAM6. *J. Adv. Model. Earth Syst.*, **5**, 146–172, <https://doi.org/10.1002/jame.20015>.
- Taguchi, M., 2010: Observed connection of the stratospheric quasi-biennial oscillation with El Niño–Southern Oscillation in radiosonde data. *J. Geophys. Res.*, **115**, D18120, <https://doi.org/10.1029/2010JD014325>.
- Watanabe, S., and Y. Kawatani, 2012: Sensitivity of the QBO to mean tropical upwelling under a changing climate simulated by an Earth system model. *J. Meteor. Soc. Japan*, **90A**, 351–360, <https://doi.org/10.2151/jmsj.2012-A20>.
- , and Coauthors, 2011: MIROC-ESM 2010: Model description and basic results of CMIP5-20c3m experiments. *Geosci. Model Dev.*, **4**, 845–872, <https://doi.org/10.5194/gmd-4-845-2011>.
- Xie, P., and P. A. Arkin, 1997: Global precipitation: A 17-year monthly analysis based on gauge observations, satellite estimates, and numerical model outputs. *Bull. Amer. Meteor. Soc.*, **78**, 2539–2558, [https://doi.org/10.1175/1520-0477\(1997\)078<2539:GPAYMA>2.0.CO;2](https://doi.org/10.1175/1520-0477(1997)078<2539:GPAYMA>2.0.CO;2).
- Yoo, C., and S.-W. Son, 2016: Modulation of the boreal wintertime Madden-Julian oscillation by the stratospheric quasi-biennial oscillation. *Geophys. Res. Lett.*, **43**, 1392–1398, <https://doi.org/10.1002/2016GL067762>.
- Yuan, W., M. A. Geller, and P. T. Love, 2014: ENSO influence on QBO modulations of the tropical tropopause. *Quart. J. Roy. Meteor. Soc.*, **140**, 1670–1676, <https://doi.org/10.1002/qj.2247>.